

Triggering Collapse of the Presolar Dense Cloud Core and Injecting Short-Lived Radioisotopes with a Shock Wave. I. Varied Shock Speeds

Alan P. Boss¹, Sandra A. Keiser¹, Sergei I. Ipatov^{1,2}, Elizabeth A. Myhill^{1,3}, and Harri A. T. Vanhala^{1,4}

ABSTRACT

The discovery of decay products of a short-lived radioisotope (SLRI) in the Allende meteorite led to the hypothesis that a supernova shock wave transported freshly synthesized SLRI to the presolar dense cloud core, triggered its self-gravitational collapse, and injected the SLRI into the core. Previous multidimensional numerical calculations of the shock-cloud collision process showed that this hypothesis is plausible when the shock wave and dense cloud core are assumed to remain isothermal at ~ 10 K, but not when compressional heating to ~ 1000 K is assumed. Our two-dimensional models (Boss et al. 2008) with the FLASH2.5 adaptive mesh refinement (AMR) hydrodynamics code have shown that a 20 km/sec shock front can simultaneously trigger collapse of a $1 M_{\odot}$ core and inject shock wave material, provided that cooling by molecular species such as H_2O , CO , and H_2 is included. Here we present the results for similar calculations with shock speeds ranging from 1 km/sec to 100 km/sec. We find that shock speeds in the range from 5 km/sec to 70 km/sec are able to trigger the collapse of a $2.2 M_{\odot}$ cloud while simultaneously injecting shock wave material: lower speed shocks do not achieve injection, while higher speed shocks do not trigger sustained collapse. The calculations continue to support the shock-wave trigger hypothesis for the formation of the solar system, though the injection efficiencies in the present models are lower than desired.

Subject headings: hydrodynamics – instabilities – solar system: formation – stars: formation

¹Department of Terrestrial Magnetism, Carnegie Institution of Washington, 5241 Broad Branch Road, NW, Washington, DC 20015-1305; boss@dtm.ciw.edu, keiser@dtm.ciw.edu.

²Catholic University, Washington, DC 20064; siipatov@hotmail.com.

³Marymount University, Arlington, VA 22207; elizabeth.myhill@marymount.edu.

⁴NCESSSE, Washington, DC 20791; HarriVanhala@ncesse.org.

1. Introduction

Triggering the collapse of the presolar cloud with an interstellar shock wave propagating away from a site of stellar nucleosynthesis is a favored explanation for the widespread evidence of short-lived radioisotopes (SLRI) in chondritic refractory inclusions (Lee et al. 1976; Cameron and Truran 1977; MacPherson, Davis and Zinner 1995) and, much more rarely, in chondrules (Russell et al. 1996) found in primitive meteorites. The goal of this paper is to continue the theoretical exploration of the triggering and injection scenario for SLRIs, in the context of shock waves striking a dense molecular cloud core that could have collapsed to form the solar system.

1.1. Short-Lived Radioisotopes

The dozen or so confirmed (^{10}Be , ^{41}Ca , ^{26}Al , ^{60}Fe , ^{53}Mn , ^{107}Pd , ^{182}Hf , ^{129}I , and ^{244}Pu) or suspected (^{99}Tc , ^{36}Cl , ^{205}Pb , and ^{92}Nb) short-lived radioisotopes may require a fairly involved history for their complete explanation (Goswami and Vanhala 2000; Meyer and Clayton 2000; McKeegan & Davis 2003; Wadhwa et al. 2007). A stellar nucleosynthetic source (a supernova or an AGB star) has been the leading explanation for most of these nuclei (Cameron 1993, 2001; Wasserburg et al. 1994, 1995, 1998; Trigo-Rodríguez et al. 2009; Huss et al. 2009), though there are other possibilities as well, in particular local production (i.e., in the solar nebula) of short-lived radioisotopes produced during spallation reactions involving energetic particles emanating from protosolar flares (Shu et al. 1997). Such local irradiation models appear to have a problem with being able to match the observed abundance ratio of ^{26}Al to ^{41}Ca (Srinivasan et al. 1996; Sahijpal et al. 1998; Lee et al. 1998). The observed abundance of ^{26}Al thus seems to require its production by stellar nucleosynthesis (McKeegan et al. 2000). However, this problem can be avoided by assuming that the refractory inclusions are shielded by a less refractory mantle during the irradiation, with the mantle being lost later on during heating of the inclusions, thereby yielding the approximate abundance ratio of ^{26}Al to ^{41}Ca observed in certain meteorites (Gounelle et al. 2001). On the other hand, producing ^{26}Al by multiple episodes of local irradiation would negate its use as a precise chronometer for the early solar system (Bizzarro et al. 2004; Halliday 2004; Krot et al. 2005; Thrane et al. 2006), which seems to be ruled out by the agreement of ^{26}Al ages with those derived from the Pb-Pb dating system (Connelly et al. 2008).

Evidence has also appeared for the presence of the short-lived isotope ^{10}Be in an Allende inclusion (McKeegan et al. 2000). Because ^{10}Be is thought to be produced only by nuclear spallation reactions, its existence has been used to argue strongly in favour of local irradiation (McKeegan et al. 2000; Gounelle et al. 2001). Sahijpal & Gupta (2009) have calculated

that even if all of the ^{10}Be was produced by local irradiation, then the amount of ^{26}Al also produced by local irradiation was about 10% of the total amount of ^{26}Al , so that the bulk of the ^{26}Al was probably synthesized by a massive star. However, if irradiation is responsible for the ^{10}Be , it is unclear if the irradiation occurred in the solar nebula, or in an earlier phase of evolution. Arnould et al. (2000) point out that spallation can occur in the winds ejected from H-depleted Wolf-Rayet (WR) stars. Desch et al. (2004) showed that the ^{10}Be might well have originated from ^{10}Be galactic cosmic rays that were stopped in the presolar cloud. Evidence has also been advanced for the presence of live ^7Be in Ca,Al-rich, refractory inclusions (CAIs), which are believed to represent the earliest solids formed in the solar nebula that have survived relatively unaltered (Chaussidon et al. 2006). Because of the extremely short half-life of ^7Be of 53 days, this evidence, if correct, would require formation of ^7Be in the solar nebula. Desch & Ouellette (2006) have disputed the ^7Be claim, which has not been confirmed by other groups to date.

The short-lived isotope ^{60}Fe (Goswami and Vanhala 2000) cannot be produced in the appropriate amounts by spallation, and requires a stellar nucleosynthetic source (Tachibana & Huss 2003), as does the bulk of the ^{26}Al observed to be polluting the interstellar medium. The half-life of ^{60}Fe is 2.6 million years (Rugel et al. 2009), roughly four times that of ^{26}Al , so in any case, the evidence for live short-lived isotopes in refractory inclusions seems to require that no more than about 1 million years elapsed between the nucleosynthesis of some of the short-lived isotopes in a star and the formation of refractory inclusions in the solar nebula.

Solar-type stars are believed to form from the collapse of dense molecular cloud cores, which are supported against collapse primarily by magnetic fields (e.g., Mouschovias, Tassis, & Kunz 2006), though turbulence also plays a role (e.g., Kudoh & Basu 2008). Collapse of a quiescent cloud core begins once the magnetic field support decreases sufficiently through the process of ambipolar diffusion. Recently Kunz & Mouschovias (2009) have shown that ambipolar diffusion leading to collapse and fragmentation is able to reproduce the observed distribution of molecular cloud core masses, i.e., the initial core mass function, suggesting the importance of magnetic fields for star formation in general. Ambipolar diffusion is estimated to require of order 10 Myr to lead to collapse (Mouschovias, Tassis, & Kunz 2006), a period considerably longer than the half-life of ^{26}Al of 0.73 Myr. If the Solar System's ^{26}Al was produced in a massive star, it may have been injected promptly into the protosolar cloud, which must have then collapsed and formed cm-sized solids, all within ~ 1 Myr. This constraint assumes that the same stellar outflow that carried the ^{26}Al may have triggered the collapse of the protosolar cloud and injected other newly-synthesized elements, including other short-lived isotopes (Cameron & Truran 1977; Boss 1995). Abundant observational support exists for the triggering of star formation by expanding supernova shells in Upper

Scorpius (Preibisch & Zinnecker 1999; Preibisch et al. 2002) and the Cygnus Loop (Patnaude et al. 2002), by superbubbles in OB associations (Oey et al. 2005; Lee & Chen 2009), by ionization fronts associated with HII regions (Leppanen, Liljestrom, & Diamond 1998; Healey, Hester, & Claussen 2004; Hester & Desch 2005; Snider et al. 2009), by generic external shocks (Tachihara et al. 2002), and by protostellar outflows (Barsony et al. 1998; Sandell & Knee 2001; Yokogawa et al. 2003). Here we consider generic shocks, with a special emphasis on supernovae and AGB stars as shock sources.

1.2. Injection Scenarios

Boss (1995) showed that shock fronts from a nearby AGB star or a relatively distant supernova could trigger the collapse of a 3D dense cloud core and inject shock front material into the collapsing cloud. Foster & Boss (1996, 1997) studied this process in greater detail for axisymmetric, 2D clouds, and pointed out the crucial role of the assumed isothermal shock front for achieving both goals of triggered collapse and injection. A supernova shock passes through three phases: ejecta-dominated, Sedov blast wave, and radiative (Chevalier 1974). The latter phase occurs at distances of about 10 pc, after which the shock front sweeps up a cool shell of gas and dust as it propagates. Several recent AMR studies (Nakamura et al. 2006; Melioli et al. 2006) have confirmed the results of Boss (1995) and Foster & Boss (1996, 1997) that shock-triggered star formation is likely to occur when the supernova shock front has evolved into a radiative shock, i.e., the shock front is able to cool so rapidly by radiation that the thin shock front gas is essentially at the same temperature as the ambient gas, which is the same situation as in the isothermal shocks considered by Boss (1995) and Foster & Boss (1996, 1997).

Rayleigh-Taylor (R-T) fingers were identified as the physical mechanism for achieving injection of dust grains and gas into the collapsing presolar cloud (Foster & Boss 1997; Vanhala & Boss 2000, 2002). Because the R-T fingers strike the outermost layers of the presolar cloud, inducing collapse, the R-T fingers do not reach the central regions until shortly after the central protosun and the early solar nebula have formed, possibly explaining the lack of ^{26}Al in certain (Fraction Unknown Nuclear = FUN) refractory inclusions (Sahijpal & Goswami 1998) that may have formed before the R-T fingers arrived. Boss (2007) modeled the R-T finger injection process in the context of this scenario simply by imagining spraying the ^{26}Al onto the surface of an existing solar nebula.

A related but alternative scenario involves having a nearby (~ 0.1 pc) supernova inject ^{26}Al directly into the solar nebula (rather than into the presolar cloud), as studied by Ouellette, Desch & Hester (2007). They found that the gas from a shock front could not

be injected efficiently into a protoplanetary disk because of the disk’s much higher density compared to the presolar cloud. Chevalier (2000) had found the same result and attributed it to the hot shock gas not having enough time to cool down. As a result, Ouellette et al. (2007) suggested that the ^{26}Al resided primarily in dust grains that shot through the stalled shock-front gas and thereby penetrated into the disk. Dust grains smaller than 0.1 micron would be deflected, but micron-sized and larger dust grains would be injected with a high efficiency (Ouellette et al. 2009).

Supernovae are known to produce large amounts of dust grains, but theoretical models suggest that the newly condensed grains are essentially all smaller than 0.1 micron, and are sputtered to even smaller sizes in the reverse shock front driven into the expanding supernova remnant (SNR) by the interstellar medium that the SNR encounters (Bianchi & Schneider 2007). The models are in accord with dust extinction estimates for an observed reddened QSO. An insignificant fraction of the total dust grain mass is contained in grains larger than 0.1 micron, presenting a problem for scenarios that rely on large dust grains for injection. However, Nittler (2007) has argued that a sub-class of presolar grains appears to have been formed in a single supernova, conceivably the same supernova that produced many SLRIs. These presolar grains have sizes of 0.1 to 10 micron, large enough to be injected into the disk, or the presolar cloud core. What fraction of the mass of the initial dust grain population these relatively large grains represent is difficult to determine, given the processing associated with detecting presolar grains in meteorites and the typical limitation to the study of grains larger than about 0.1 micron (e.g., Amari, Lewis, & Anders 1994).

Recently it has been suggested that ^{60}Fe was injected by a supernova directly into the solar nebula roughly 1 Myr after Solar System formation (Bizzarro et al. 2007), as in the Ouellette et al. (2007) models. In this scenario, the ^{26}Al was derived from the wind from a Wolf-Rayet (WR) star, a massive star that would later become a supernova and inject the ^{60}Fe . WR winds do indeed carry large amounts of ^{26}Al (Arnould, Goriely, & Meynet 2006), with winds that are comparable in speed (~ 1500 km/sec) to supernova shocks (Marchenko et al. 2006), meaning that such winds would need to be slowed down by sweeping up interstellar gas and dust to speeds less than ~ 40 km/sec if they are to trigger cloud collapse rather than simply shred clouds to pieces (Foster & Boss 1996, 1997). However, other groups have not been able to replicate the Ni isotope data that forms the basis for the ^{60}Fe scenario (Dauphas et al. 2008; Regelous et al. 2008). Nevertheless, WR stars should be considered as a possible source of ^{26}Al in addition to that obtained from a supernova (e.g., Gaidos et al. 2009).

Williams & Gaidos (2007) estimated that the likelihood of a protoplanetary disk being struck by a supernova shock was less than 1%, but considering that we do not know if the

Solar System’s inventory of short-lived isotopes is rare or not, such an argument cannot be considered decisive. In fact, it has been argued recently that significant ^{26}Al is necessary for the development of technological civilizations (Gilmour & Middleton 2009). However, Gounelle & Meibom (2007) and Krot et al. (2008) argued that injection could not have occurred directly onto a relatively late-phase, low mass solar nebula, as ^{26}Al from a massive star supernova would have been accompanied by sufficient oxygen to lead to an oxygen isotope distribution in the solar nebula that would be distinct from that inferred for the sun based on mass-independent fractionation of carbonaceous chondrites and from that recently measured by the Genesis Mission (McKeegan et al. 2008). Krot et al. (2008) therefore argued that injection must have instead occurred into the presolar cloud, so that the sun and the solar nebula shared a common reservoir of oxygen isotopes that could then undergo fractionation. Ellinger, Young, & Desch (2009), however, pointed out that supernova explosions are not spherically symmetric, and so some degree of anisotropy in the ejecta is to be expected, perhaps enough to permit ^{26}Al injection into the presolar nebula without disturbing the oxygen isotope ratios.

1.3. Shock Thermodynamics

While isothermal shock fronts are capable of simultaneous triggering and injection (Boss 1995; Foster & Boss 1996, 1997; Vanhala & Boss 2000, 2002), it has been less clear what happens when detailed heating and cooling processes in the shock front are considered. Vanhala and Cameron (1998) found that when they allowed nonisothermal shocks in their models, they could not find a combination of target cloud and shock wave parameters that permitted both triggered collapse and injection to occur: they could trigger cloud collapse, or they could inject particles, but not both in the same simulation. Such an outcome would be fatal to the triggering and injection hypothesis if definitive. However, Vanhala & Cameron’s (1998) models employed a smoothed-particle hydrodynamics (SPH) code, which has since been shown to be poor at resolving dynamical instabilities such as the Rayleigh-Taylor or Kelvin-Helmholtz instabilities (Agertz et al. 2007). Furthermore, Vanhala and Cameron’s (1998) thermodynamical routines led to post-shock thermal profiles that were quite different from those of Kaufman & Neufeld (1996), who found that for a 40 km/sec shock, the post-shock gas cooled down from a maximum of over 3000 K to less than 100 K within a distance of 0.001 pc. With a 25 km/sec shock in the Vanhala & Cameron (1996) SPH code, however, the post-shock temperature rose to 3000 K and showed no signs of decreasing over a distance on the order of 0.5 pc.

Kaufmann & Neufeld (1996) studied C-type shock fronts, which result in the most suc-

cessful models of the shock emission from the Kleinmann-Low nebula in the Orion molecular cloud. Kaufman & Neufeld (1996) assumed preshock magnetic field strengths in their C-shock models that are consistent with magnetic field strengths measured by Zeeman splitting in molecular clouds (Crutcher 1999). Such nondissociative, magnetohydrodynamic C-type shocks appear to be the correct analogue for the shock speeds (~ 5 to 40 km s^{-1}) that we expect will be necessary to simultaneously achieve triggered collapse and injection. The relatively low postshock temperatures in C-type shocks are crucial for this scenario. Postshock cooling depends sensitively on the detailed microphysics, e.g., on the emission from rotational states of H_2O , H_2 , CO , and OH , and hence on quantities such as the ratio of ortho- to para-hydrogen molecules (Neufeld & Kaufmann 1993; Kaufmann & Neufeld 1996). Atomic species are also important coolants, as are dust grains. More recently Morris, Desch, & Ciesla (2009) have reexamined the question of cooling shocked gas by H_2O line emission, finding that the cooling rates in the optically thin limit are at least as high as those calculated by Neufeld & Kaufmann (1993).

Boss et al. (2008) found that simultaneous triggering and injection was possible for a 20 km/sec shock striking a $1 M_\odot$ cloud, provided that Neufeld & Kaufmann’s (1993) molecular cooling functions were employed. Gounelle et al. (2009) interpreted this result as meaning that only a very narrow range of shock speeds was consistent with the triggering and injection hypothesis. In this paper we examine what happens for a wide range of shock speeds (and different mass clouds) compared to the single shock speed considered by Boss et al. (2008), in order to determine the robustness of the shock wave trigger hypothesis.

2. Numerical Methods

Achieving adequate spatial resolution of shock-compressed regions of presolar clouds hit with supernova shock fronts, while minimizing the overall computational burden, is an insurmountable problem for a fixed grid hydro code of the type previously used on these problems (Boss 1995; Foster & Boss 1996, 1997; Vanhala & Boss 2000, 2002). Clearly the demands of the shock-triggered collapse and injection problem requires adoption of the Adaptive Mesh Refinement (AMR; e.g., Truelove et al. 1997; Poludnenko et al. 2002) technique, which was designed to handle just this type of situation. AMR techniques automatically insert new grid points in regions of strong physical gradients, and remove them in regions without strong gradients, in order to maximize the spatial resolution in the crucial regions while minimizing the computational burden.

FLASH employs a block-structured adaptive grid approach using the PARAMESH package. Advection is handled by the piecewise parabolic method (PPM), which features a Rie-

mann solver at cell boundaries that handles shock fronts exceptionally well. In FLASH, PPM is incorporated in a form that is second-order accurate in space and time. We have tested the FLASH2.5 code’s ability to reproduce the results of several different test cases that are relevant to the problem of triggering cloud collapse, namely the Sod shock tube problem and the collapse of a pressureless sphere. While the performance of FLASH on the pressureless sphere collapse is not as accurate as with codes designed to study collapse problems (e.g., Boss & Myhill 1992), FLASH does a superb job of handling the Sod shock tube problem on a Cartesian grid, when the shock flows parallel to one axis or at a 45 degree angle. While the standard FLASH test cases were run on Cartesian grids, we have also reproduced the correct results for the Sod shock tube and for pressureless cloud collapse on the cylindrical coordinate (R, Z) grid that is used in the present calculations.

In the absence of cooling or an isothermal constraint, FLASH produces an adiabatic evolution with an effective $\gamma = 5/3$. The FLASH equation of state routines were taken to be those for a simple perfect gas with a mean molecular weight of $\mu = 2.3$. We have adapted these FLASH routines to simulate isothermal shock-cloud interactions, where the entire computational grid is forced to remain isothermal, typically at 10 K, in order to compare with the results of Foster & Boss (1996). In these models, γ is set equal to 1.01, as a value of $\gamma = 1.0$ is prohibited by the Riemann solver.

In addition to isothermal models, we also present models that employed the same compressional heating and radiative cooling that was studied by Boss et al. (2008). Our model for radiative cooling is based on the results of Neufeld & Kaufman (1993), who calculated the radiative cooling caused by rotational and vibrational transitions of optically thin, warm molecular gas composed of H_2O , CO , and H_2 and found H_2O to be the dominant cooling agent. Neufeld & Kaufman’s (1993) Figure 3 shows that over the range of temperatures from 100 K to 4000 K, the total cooling rate coefficient L can be approximated as $L \approx L_0 \approx 10^{-24}(T/100) \text{ erg cm}^3 \text{ s}^{-1}$. The cooling rate $\Lambda = L n(H_2) n(m)$, where $n(H_2)$ is the number density of hydrogen molecules and $n(m)$ is the number density of the molecular species under consideration. Assuming that $n(H_2O)/n(H_2) \approx 8.8 \times 10^{-4}$ (Neufeld & Kaufman 1993), we take $n(m)/n(H_2) \approx 10^{-3}$, leading to a radiative cooling rate of $\Lambda \approx 9 \times 10^{19}(T/100)\rho^2 \text{ erg cm}^{-3} \text{ s}^{-1}$, where ρ is the gas density in g cm^{-3} . Boss et al. (2008) found that Λ could be increased or decreased by factors of two without having a major effect on the outcome of shock triggering and injection, so the precise value of Λ does not appear to be critical to the results.

Kaufman & Neufeld (1996) found that the peak temperatures in their MHD shocks were typically of order 1000 K for shock speeds in the range from 5 km/sec to 45 km/sec. As a result, the temperatures in the present models as well as those of Boss et al. (2008) have

been restricted to values between 10 K and 1000 K. Kaufman & Neufeld (1996) also found a typical shock thickness of order $0.001 \text{ pc} = 3 \times 10^{15} \text{ cm}$ for a 40 km/sec shock propagating in a magnetized gas with a preshock density similar to that of dense cloud cores. A similar shock thickness occurs in the models of Boss et al. (2008), using the Neufeld & Kaufman (1993) radiative cooling rate Λ , though with a 20 km/sec shock speed and an unmagnetized cloud: evidently the higher shock speed in Kaufman & Neufeld (1996) is roughly compensated for by the presence of magnetic fields, compared to the Boss et al. (2008) results.

As in Boss et al. (2008), in the present models we used the two dimensional, cylindrical coordinate (R, Z) version of FLASH2.5, with axisymmetry about the rotational axis (\hat{z}). Multipole gravity was used, including Legendre polynomials up to $l = 10$. The cylindrical grid is typically 0.197 pc long in Z and 0.063 pc wide in R , though in the higher shock speed models, the grid was extended to be 0.320 pc long in order to better follow the interaction. We set the number of blocks in R (N_{BR}) to be 5 in all cases, while the number of blocks in Z (N_{BZ}) has been varied from 5 to 20. Most models have had 15 blocks in Z , leading to an approximately uniform grid spacing in R and Z . With each block consisting of 8×8 grid points, this is equivalent to an initial grid of 40×120 for most models. The number of levels of refinement (N_L) has been varied from five to six. With five levels of refinement employed, FLASH is able to follow small-scale structures with the effective resolution of a grid 16 times finer in scale, or effectively 640×1920 , somewhat better than the highest resolution of 480×1440 used by Vanhala & Boss (2000). With six levels, the resolution is increased by another factor of two in each direction.

3. Initial Conditions

Our target dense cloud cores consist of Bonner-Ebert (BE) spheres (Bonnor 1956), which are the equilibrium structures for self-gravitating, isothermal spheres of gas. BE spheres are excellent models for the structure of pre-collapse dense molecular cloud cores seen in star-forming regions (e.g., Shirley et al. 2005). For the models that compare results to the isothermal models of Foster & Boss (1996, 1997), the target dense cloud core is a BE sphere with a mass of $1.1 M_{\odot}$, a radius of 0.058 pc, a temperature of $T = 10 \text{ K}$, and a maximum density of $6.2 \times 10^{-19} \text{ g cm}^{-3}$, located at rest near the top of the cylindrical grid. The BE sphere is embedded in an intercloud medium with a density of $3.6 \times 10^{-22} \text{ g cm}^{-3}$ and a temperature of 10 K. The shock wave begins at the top of the grid and propagates downward at a specified speed toward the BE sphere. The shock wave has a thickness of 0.003 pc with a uniform density of $3.6 \times 10^{-20} \text{ g cm}^{-3}$, a mass of $0.016 M_{\odot}$, and a temperature of 10 K. For the models where cooling is included, the shock wave begins with a temperature of 1000 K

and is followed by a post-shock wind with a density of $3.6 \times 10^{-22} \text{ g cm}^{-3}$ and temperature of 1000 K, also moving downward at the same speed as the shock wave.

The assumed shock structure is the same as that used in the standard case of Foster & Boss (1996, 1997) and investigated by Boss et al. (2008). The shock structure was chosen to resemble the expected conditions in a planetary nebula wind (e.g., Plait & Soker 1990; see discussion in Foster & Boss 1996). However, it is also consistent with a supernova shock that has swept-up considerable material and slowed down as a result. Chevalier (1974) considered a supernova shock propagating into a cold ($T = 10 \text{ K}$) medium with a number density of 1 cm^{-3} . By 0.25 Myr, the shock has slowed to a top speed of $\sim 60 \text{ km/sec}$ and has travelled a distance of $\sim 2.5 \text{ pc}$. The amount of swept-up mass contained in the shock front that is incident on the target clouds used in the present calculations is $0.015 M_{\odot}$, quite close to the value of $0.016 M_{\odot}$ in the standard case.

The shock wave material is represented by a color field, initially defined to be equal to 1 inside the shock wave and 0 elsewhere, which allows the shock wave material to be tracked in time (Foster & Boss 1997). The SLRI are assumed to be contained primarily in dust grains of sub-micron size (e.g., Bianchi & Schneider 2007), small enough for the grains to remain coupled to the gas. Grains larger than this size could shoot through the shock front as it strikes the target cloud and increase the injection efficiency (e.g., Ouellette et al. 2007, 2009), so injection efficiencies derived solely from the color field approach should be considered as lower bounds on the true injection efficiencies.

4. Results

We present results for several related studies with the FLASH code, namely a set of comparisons with the results on the standard case of Foster & Boss (1996, 1997), the stability of BE-like spheres with higher central densities (and higher masses) in the absence of shock waves, and, finally, the effects of varying the shock wave speed across a wide range of values for a BE-like target sphere with a mass of $2.2M_{\odot}$.

4.1. Standard Case Comparisons

We first used FLASH2.5 to reproduce the standard case of triggered isothermal collapse of Foster & Boss (1996), and verified that FLASH2.5 was able to produce simultaneous triggered collapse and injection of shock wave material in the case of a 20 km/sec shock.

Table 1 lists four models that duplicate the standard case, with varied spatial resolution

in FLASH2.5. Table 1 also gives the results of the models: the maximum density obtained (ρ_{max}) in g cm^{-3} , the fraction of the incident color field that is injected (f_i), and the final time of the model (t_f) in seconds. Once maximum densities of $\sim 10^{-12} \text{ g cm}^{-3}$ are reached, even with five or six levels of refinement, FLASH is unable to follow the collapse to even higher densities, either because it does not have sufficient spatial resolution on the scale of the density maximum, which typically occupies only a few grid cells, or else because the Poisson solver is unable to properly represent the gravitational potential of what has become in essence a point mass. As a result, the final times listed in Table 1 do not correspond to the time when the density maximum is reached, as FLASH simply continues to do its best to evolve the entire cloud-shock system past that instant of time. Once maximum densities of $\sim 10^{-12} \text{ g cm}^{-3}$ are reached, it is appropriate to terminate these calculations anyway, because by such densities the collapsing cores have become optically thick and can no longer cool by our assumed molecular cooling law, which assumes optically thin clouds. A full radiative transfer treatment (e.g., Boss & Myhill 1992) is required to treat optically thick regions, a capability that does not exist in FLASH2.5. Finally, as in Boss et al. (2008), f_i is defined to be that fraction of the initial color field that is incident on the initial target cloud and that is injected into regions of the collapsing cloud core with density greater than $10^{-18} \text{ g cm}^{-3}$. That is to say, if the total amount of color that is incident on the target cloud is 1 in dimensionless units, $f_i = 0.001$ means that 0.001 is the amount of color that was injected.

It is clear from Table 1 that in all four models, the BE sphere was triggered into self-gravitational collapse, given that maximum densities of $\sim 10^{-12} \text{ g cm}^{-3}$ or higher were achieved in each case. This maximum density is well over a factor of 10^6 times higher than the initial maximum density in the target BE sphere of $6.2 \times 10^{-19} \text{ g cm}^{-3}$, indicating that dynamical collapse has been induced in these cloud cores. It is also clear that as the spatial resolution in FLASH is increased, the collapsing cloud is able to reach slightly higher densities, implying that the highest resolution calculations are approaching the continuum limit. Note also that the injection efficiency obtained for model FBD, 0.002, is only slightly lower than the efficiency of 0.003 obtained for the 20 km/sec shock model with heating and cooling presented by Boss et al. (2008), which had the same spatial resolution as model FBD, showing that when nonisothermal processes are considered, the injection process becomes only somewhat less efficient than when isothermality is assumed.

The evolution of these four isothermal models is very similar to that of the models to be presented below with compressional heating and radiative cooling, and so separate figures for the isothermal models are not displayed.

4.2. Stability of Varied Mass Spheres

We have also used FLASH to verify the long-term stability of the target clouds in the absence of a triggering shock front, as clouds that collapse on their own on time scales similar to the shock wave passage cannot be considered to have been triggered into collapse. Shocked-triggered collapse for the standard case occurs within a time span of about 10^5 yrs (Foster & Boss 1996, 1997; Boss et al. 2008). When the target BE sphere used in the models in Table 1 is evolved isothermally in FLASH2.5 without being struck by a shock wave, it does not collapse, but instead oscillates around its initial equilibrium structure, over a time period of at least 10^6 yrs, sufficiently long to validate the claim that triggering has occurred in the Foster & Boss (1996) comparison models.

In addition, we have tested the stability of higher mass cloud cores, obtained simply by multiplying the initial densities of the standard case BE sphere by factors of 2, 3, or 4. Formally speaking, these clouds are not true BE spheres in equilibrium, but any deleterious effects of this simple computational convenience can be discerned by seeing if the clouds do indeed collapse on their own without being subjected to shock triggering. In the case of the two clouds where the densities had been increased by factors of 3 or 4, the clouds did indeed begin to undergo dynamic collapse to densities of $\sim 10^{-12}$ g cm $^{-3}$ or higher within times of $\sim 10^5$ yrs, showing their gravitational instability and unsuitability for the shock-triggering models. However, the cloud with twice the BE sphere density, i.e., an initial central density of 1.24×10^{-18} g cm $^{-3}$ and a mass of $2.2 M_{\odot}$, remained stable in FLASH for at least $\sim 10^6$ yrs, proving its suitability for the present studies. The next section then presents the results for when a $2.2 M_{\odot}$ cloud core is struck by shocks with varying speeds.

4.3. Varied Shock Wave Speeds

We now turn to the main focus of this paper, a consideration of what happens when shock waves with a wide variety of speeds are allowed to strike a dense cloud core, while including a fully nonisothermal treatment with compressional heating and radiative cooling.

Table 2 lists the shock speeds employed for these models of a $2.2 M_{\odot}$ target cloud core, as well as the results of the calculations, as in Table 1. Several variations on the spatial resolution were also calculated: models v4-4 and v5-4 had four levels of adaptive mesh refinement, rather than five, while model v20-6 had six. The higher speed models (v75L, v80L, v90L, and v100L) had longer grids in the Z (vertical) direction, in order to better follow the evolution of the cloud as it is swept downward by the shock front. Figure 1 depicts the initial density distribution for all of the nonisothermal models with varied shock

speeds, showing the target cloud and the incoming shock front, where the color field is taken to be initially uniform with a value of unity.

Figures 1 through 3 show the evolution of model v20, which typifies the results for models resulting in simultaneous collapse and injection. Model v20 is also identical to model C of Boss et al. (2008), except for having a cloud mass of $2.2 M_{\odot}$ instead of $1 M_{\odot}$, and behaves in a very similar manner, implying that the process works equally well for target clouds in this mass range.

Figure 2 shows that the model v20 shock front is able to compress the top edge of the target cloud, while Rayleigh-Taylor (R-T) fingers and Kelvin-Helmholtz (K-H) vortices form around the shock-cloud interface. The R-T fingers drive into the target cloud, while the K-H vortices tend to ablate material off the cloud edge and force it to join the downstream flow. The contours for the color field in Figure 2 show that most of the color field impinging on the target cloud is diverted from the cloud by these vortices and disappears downstream. Figure 4 shows a close-up of the shock-cloud interface of model v20 at the same time as Figure 2, providing a better look at the structure of the R-T and K-H features, as well as of the color field.

Figure 3 shows that model v20 is able to form a dense clump along the symmetry axis less than 0.1 Myr after the evolution began. Figure 5 shows a close-up of the dense clump at the same time as Figure 3, this time with the temperature field contoured in black, instead of the color field. Temperatures rise above 100 K only in regions immediately adjacent to the shock-cloud interface, i.e., in the region with the largest density gradients and hence the strongest compressional heating. Except for this highly shocked region, then, the bulk of the cloud is able to remain nearly isothermal at the assumed background temperature of 10 K as a result of the cooling by molecular species such as H_2O , CO , and H_2 . The strength of this molecular cooling explains why the results of the nonisothermal model presented by Boss et al. (2008) are so similar to those of the isothermal standard test case of Foster & Boss (1996, 1997).

Figure 6 shows an even closer-in view of the density maximum of model v20 after a time of 0.1 Myr. The velocity vectors indicate that the region in the vicinity of the density maximum is trying to collapse onto the clump with speeds as high as several km/sec, which is highly supersonic, considering that the sound speed in 10 K gas is 0.2 km/sec. Evidently, a protostar with a maximum density of $\sim 10^{-13} \text{ g cm}^{-3}$ has formed and is growing by the accretion of gas from the target cloud’s envelope. Meanwhile, the protostar has been accelerated by the shock front to a speed of order 1 km/sec, and is moving downward as a result. Figure 7 plots the color field over the same region as Figure 6, showing that significant shock front material has been injected into the collapsing protostar and the infalling cloud enve-

lope. Multiple waves of shock front material should be accreted by the protostar, considering the velocity field evident in Figure 7, including the regions with even higher color densities than that within the density maximum, which appear likely to collapse onto the protostar within a few thousand more years.

Figure 8, 9, and 10 show the evolution of model v4, where dynamic collapse was triggered, but no significant injection occurred. Comparing Figure 8 for model v4 with Figure 2 for model v20, at comparable phases of shock-cloud interaction, it is apparent that the much slower speed shock front in model v4 is unable to compress the target cloud’s edge to the extent achieved by the shock in model v20. In fact, by a time of 0.105 Myr (Figure 9), the cloud in model v4 has been clearly triggered into collapse by the shock front, yet the color field lags behind and seems unlikely to achieve a significant injection efficiency. Figure 10 depicts a close-up of the density maximum for model v4 at the same time as in Figure 9, showing that the cloud has been triggered into roughly spherically symmetric collapse, judging from the density distribution and the velocity vectors. At the same time, the color field within the region plotted in Figure 10 is essentially zero, implying that if any shock front material is to be accreted by the growing protostar, it must occur at some later phase in its evolution.

Finally, Figures 11, 12, and 13 show the evolution for model v80L, where injection occurred, but dynamical collapse did not ensue. In this case, the strong shock front tends to shred the target cloud into streamers (Figure 11), an excellent situation for injecting shock-front material into the same region (Figure 12), but not well-suited for inducing sustained dynamic collapse. Model v80L achieved a maximum density of $\sim 10^{-15}$ g cm $^{-3}$ by the time shown in Figure 11 of 0.056 Myr, and by 0.1 Myr (Figure 13), the maximum density has dropped to $\sim 10^{-16}$ g cm $^{-3}$. Figure 12 also demonstrates that even with the more vigorous shock compressional heating in model v80L, the molecular cooling is able to limit the shock-heated regions to the close vicinity of the shock-cloud boundary.

In summary, Figure 14 shows how the critical outcomes of achieving injection and sustained collapse depend on the assumed shock speed, for all the models listed in Table 2. Low speed shocks can induce collapse, but not injection, while high speed shocks result in significant injection, but not in collapse. Shocks falling in the range of about 5 km/sec to 70 km/sec appear to be able to simultaneously induce collapse and achieve injection of significant amounts of shock wave material. This result is consistent with the prediction by Foster & Boss (1996) that shock speeds of ~ 100 km/sec or higher would shred the target clouds and prevent the formation of a collapsing protostar.

Table 2 also shows that these basic results are relatively insensitive to the amount of spatial resolution employed, specifically to the number of AMR grid levels allowed. Model

v5 with the standard 5 levels of AMR and model v5-4 with 4 levels resulted in quite similar outcomes, as was the case for model v20 with 5 levels and model v20-6 with 6 levels.

4.4. Injection Efficiencies

Boss et al. (2008) found that for a $1.0 M_{\odot}$ target cloud and a 20 km/sec shock, the injection efficiency f_i was 0.003. For the comparable $2.2 M_{\odot}$ target cloud in model v20, f_i was 0.001, a factor of three times lower for the higher mass cloud. This difference may be attributed to the fact that while the shock front was identical in both models, the larger mass of the target cloud in model v20 made the task of the shock front more difficult: evidently somewhat lower mass clouds are easier to trigger into collapse and pollute with shock front material than somewhat higher mass clouds, at least to the phase studied by these models (i.e., maximum densities less than $\sim 10^{-12}$ g cm $^{-3}$).

Estimates of the injection efficiency f_i have dropped steadily as the spatial resolution and physical modeling have improved. Boss (1995) found that about half of the impinging shock material ($f_i = 0.5$) entered the collapsing cloud in his coarsely-gridded, 3D isothermal models. Foster & Boss (1997) found f_i between 0.1 and 0.2 in their relatively coarsely-gridded, 2D isothermal models, while Vanhala & Boss (2000, 2002) found $f_i \sim 0.1$ in their increasingly higher spatial resolution, 2D isothermal models.

Broadly speaking, a typical value of $f_i \sim 0.001$ characterizes all of the successful triggering and injection models listed in Table 2, a value considerably lower than those previously found. This difference may be attributed to a number of factors, principally the improved spatial resolution of the current models and the inclusion of nonisothermal heating effects, both of which appear to have the effect of reducing f_i compared to lower resolution, isothermal calculations. The superior shock-handling ability of the PPM hydrodynamics method that FLASH is based upon undoubtedly also plays a role. Finally, there is the question of how f_i is defined, and when it is evaluated: in Vanhala & Boss (2002), e.g., f_i was typically evaluated at earlier times than in the present models, and the region over which the color field was considered to have been injected was liberally interpreted to extend quite some distance from the collapsing protostar (e.g., Figure 3 in Vanhala & Boss 2002). When the region expected to be accreted by the protostar is defined in a similar manner to that used in the present models, an estimate of $f_i \sim 0.002$ results from the Vanhala & Boss (2002) models, an estimate more in line with the current values.

Nevertheless, such a low injection efficiency may still be in accord with a supernova as the source of the shock wave. Based on the estimates of Cameron et al. (1995), Foster &

Boss (1997) noted that the ^{26}Al -containing gas and dust in a supernova shock wave would have to be diluted by a factor of $\sim 10^4$ in order to explain the inferred initial abundance of ^{26}Al in the solar nebula, i.e., $10^{-4}M_{\odot}$ of supernova shock-wave material should be injected into a $1 M_{\odot}$ presolar cloud.

More recently, Takigawa et al. (2008) used detailed models of a faint supernova with mixing and fallback to attempt to match the inferred initial abundances of the SLRIs ^{26}Al , ^{41}Ca , ^{53}Mn , and ^{60}Fe in the solar nebula, based on nucleosynthetic yield calculations (e.g., Rauscher et al. 2002). They found that a dilution factor of $D \sim 10^{-4}$ and a time interval of 1 Myr between the supernova explosion and the formation of the first refractory solids in the solar nebula was able to do a good job of matching all four initial abundances. The dilution factor D is the ratio of the amount of mass derived from the supernova that ends up in the solar nebula to the amount of mass in the solar nebula that did not derive from the supernova, i.e., the mass derived from the target cloud in the present models. Takigawa et al. (2008) found that the best estimates for D depended on the assumed mass of the pre-supernova star, ranging from $D = 1.3 \times 10^{-4}$ for a $25 M_{\odot}$ star to $D = 1.9 \times 10^{-3}$ for a $20 M_{\odot}$ star; stars with masses of 30 and $40 M_{\odot}$ led to intermediate values of D . Gaidos et al. (2009), on the other hand, suggest a value of D of at least 3×10^{-3} for a $25 M_{\odot}$ progenitor star, significantly larger than the estimate by Takigawa et al. (2008).

Trigo-Rodríguez et al. (2009) have shown that a $6.5 M_{\odot}$ AGB star could have produced the inferred initial abundances of the SLRIs ^{26}Al , ^{41}Ca , ^{60}Fe , and ^{107}Pd in the solar nebula, with a similar dilution factor of $D \sim 3 \times 10^{-3}$. The planetary nebulae formed by AGB stars typically have slow wind speeds of 10 km/sec, while the fast winds caused by AGB flashes can overtake the slow winds and produce swept-up shells with speeds of 30 km/sec (Frank & Mellema 1994, their Figures 1 and 2). In fact, the swept-up shell in the Frank & Mellema (1994) model closely resembles the structure assumed for the shock front here and in the standard cases of Foster & Boss (1996, 1997): a shock front with a number density of $\sim 10^4 \text{ cm}^{-3}$ and a thickness of 10^{16} cm , leading to a total shock front mass of $0.016 M_{\odot}$ impacting the target cloud. Based on the present models, then, AGB-derived shocks moving at speeds of $\sim 30 \text{ km/sec}$ should be able to trigger collapse and injection in the same manner as a supernova shock with similar properties.

In the present models, the mass of the shock wave that is incident on the target cloud is $0.016 M_{\odot}$, so values of $f_i \sim 0.001$ imply that about $2 \times 10^{-5}M_{\odot}$ of shock front material is injected into the collapsing protostar. If the final result is a well-mixed $\sim 1M_{\odot}$ protostar and protoplanetary disk, then the dilution factor D is $\sim 2 \times 10^{-5}$, considerably lower than required by either Takigawa et al. (2008) or Gaidos et al. (2009). In fact, the mismatch is even worse than this, because in the case of a supernova shock front, the material ejected

by the supernova must be diluted by the swept-up, intervening interstellar medium that is necessary to slow down the shock front to speeds capable of achieving triggering and injection. A supernova shock launched at 1000 km/sec must snowplow at least 15 times more mass in order to slow below 70 km/sec. Hence the dilution factor for a supernova shock must be decreased by this same factor, to $D \sim 10^{-6}$.

Clearly there is a need to learn if these crudely estimated dilution factors can be increased to values closer to those advocated by Takigawa et al. (2008) or Gaidos et al. (2009). Not all of the $2.2 M_{\odot}$ target cloud will be accreted by the growing protostar, so the injection efficiency will be larger by a proportionate amount. In addition, if the bulk of the shock front material infalls somewhat later than the earliest arrivals (as suggested by the color waves in Figure 7), then the shock front material may end up preferentially in the protoplanetary disk, rather than in the star, thereby increasing proportionally the dilution factor in the disk. Since the present models do not include rotation of the target cloud or shock front, there is no possibility for a rotationally supported disk to form, and so the present models cannot fully answer the question of the dilution factor appropriate for the solar nebula, as opposed to the presolar cloud as a whole. Calculations are currently underway on the dc101 cluster at DTM that include rotation for 2D target clouds, in order to address this key question.

Given the lower injection efficiency for a $2.2 M_{\odot}$ cloud compared to a $1.0 M_{\odot}$ cloud, higher cloud densities evidently result in lower injection efficiencies, as might be expected. Target clouds with lower initial densities should then have higher injection efficiencies, and their larger radii (for a given mass cloud) will also go in the direction of increasing the total amount of injected shock wave material. Furthermore, allowing injection of shock wave material from behind the leading edge of the shock front (here considered to be only 0.003 pc thick) will also increase the amount injected. Increasing the assumed density and thickness of the shock front should also lead to higher injection efficiencies. Future work will include the study of shock fronts with different densities and thicknesses compared to the standard case of Foster & Boss (1996, 1997) and employed in the present models, as well as different density and radii target clouds, in order to better ascertain the suitability of a wider range of possible shock fronts and target clouds for triggering and injection.

Coupled with these concerns over the low injection efficiency and the dilution factor are the implications for the star-formation environment where simultaneous triggering and injection might have occurred. Looney, Tobin, & Fields (2006) showed that for the target cloud considered here and an injection efficiency of $f_i = 0.1$, due to geometric dilution alone, a supernova would have to occur within about 0.06 pc to 1.2 pc from the target cloud core in order to inject the desired amount of SLRIs. For the much lower values of f_i found here, $f_i \sim 0.001$, these distance estimates decrease by factors of 10, to 0.006 pc

to 0.12 pc. Such distances are appropriate for the proplyds in the Orion nebula that are being photoevaporated by the Orion Trapezium’s four O stars (e.g., Williams, Andrews, & Wilner 2005). However, the proplyds have already collapsed to form protostars, and the density of the surrounding HII region is too low to slow down a supernova shock wave by snowplowing to the required speeds. Thus it remains to be seen if a combination of target cloud and shock front parameters can be found that will increase the injection efficiencies sufficiently to produce a scenario that is consistent with observations of regions of high mass star formation (e.g., Hester & Desch 2005).

5. Conclusions

When cooling by appropriate molecular species is included, shocks with speeds in the range from 5 km/sec to 70 km/sec are able to trigger the gravitational collapse of otherwise stable, dense cloud cores, as well as to inject shock wave material into the collapsing cloud cores. This injected material consists of shock wave gas as well as dust grains small enough to remain coupled to the gas, i.e., sub-micron-sized grains, which are expected to characterize supernova shock waves (Bianchi & Schneider 2007) and to carry the SLRI whose decay products have been found in refractory inclusions of chondritic meteorites. Evidently a radiative-phase supernova shock wave (Chevalier 1974) is able to cool sufficiently rapidly to behave in much the same way as a shock wave that is assumed to remain isothermal with the target cloud (e.g., Boss 1995). Given that Wolf-Rayet star winds and supernova shocks both are launched with shock speeds on the order of 10^3 km/sec, these shock waves can only trigger collapse after they have travelled some distance (typically about 10 pc) and been slowed down to 5 km/sec to 70 km/sec by the snowplowing of intervening interstellar cloud gas and dust. The distance a fast shock must travel in order to slow down to speeds consistent with simultaneous triggering and injection is inversely proportional to the mean density of the intervening material (assuming this material to be moving much less than the shock speed); typical interstellar medium densities lead to distances of a few pc, depending on the desired shock speed. An AGB star wind with a typical speed of 10 to 30 km/sec could also have triggered collapse and injection without the need for snowplowing. The low injection efficiencies of the present models, however, point to the need to consider shock fronts and target clouds with different parameters, in order to learn if the injection efficiencies can be increased to the levels thought to be necessary to explain the observed abundances of fossil SLRIs in meteorites.

We are currently running three-dimensional (3D) models on the Xenia cluster at DTM. The need for a 3D treatment of the shock triggering process is evident from previous 3D

studies of the R-T instability (Stone & Gardiner 2007) and shock fronts (Stone & Norman 1992; Whalen & Norman 2008). The R-T “sheets” that form in axisymmetric 2D models become true R-T fingers in 3D, allowing better penetration into the target dense cloud cores. We will present the results of these ongoing 3D models as well as of models with varied shock fronts and target clouds in future papers.

We thank the referee, Steven Desch, for several constructive reports that have led to a number of significant improvements in this paper. The calculations were performed primarily on the dc101 cluster at DTM. This research was supported in part by NASA Origins of Solar Systems grant NNG05GI10G and NASA Planetary Geology and Geophysics grant NNX07AP46G, and is contributed in part to NASA Astrobiology Institute grant NCC2-1056. The software used in this work was in part developed by the DOE-supported ASC/Alliances Center for Astrophysical Thermonuclear Flashes at the University of Chicago.

REFERENCES

- Agertz, O., et al. 2007, MNRAS, 380, 963
- Amari, S., Lewis, R. S., & Anders, E. 1994, *Geochim. Cosmochim. Acta*, 58, 459
- Arnould, M., Goriely, S., & Meynet, G. 2006, *A&A*, 453, 653
- Arnould, M., Meynet, G., & Mowlavi, N. 2000, *Chem. Geol.*, 169, 83
- Barsony, M., et al. 1998, *ApJ*, 509, 733
- Bianchi, S., & Schneider, R. 2007, MNRAS, 378, 973
- Bizzarro, M., Baker, J. A., & Haack, H. 2004, *Nature*, 431, 275
- Bizzarro, M., et al. 2007, *Science*, 316, 1178
- Bonnor, W. B. 1956, MNRAS, 116, 351
- Boss, A. P. 1995, *ApJ*, 439, 224
- Boss, A. P. 2007, *ApJ*, 660, 1707
- Boss, A. P., et al. 2008, *ApJ*, 686, L119
- Boss, A. P., & Myhill, E. A. 1992, *ApJS*, 83, 311
- Cameron, A. G. W. 1993, in *Protostars & Planets III*, ed. E. H. Levy, J. I. Lunine, & M. S. Matthews (Tucson, AZ: Univ. Arizona Press), 47
- . 2001, *Meteor. Planet. Sci.*, 36, 9

- Cameron, A. G. W., Höflich, P., Myers, P. C., & Clayton, D. D. 1995, *ApJ*, 447, L53
- Cameron, A. G. W., & Truran, J. W. 1977, *Icarus*, 30, 447
- Chaussidon, M., Robert, F., & McKeegan, K.D. 2006, *Geochim. Cosmochim. Acta*, 70, 224
- Chevalier, R. 1974, *ApJ*, 188, 501
- . 2000, *ApJ*, 538, L151
- Connelly, J. N., Amelin, Y., Krot, A. N., & Bizzarro, M. 2008, *ApJ*, 675, L121
- Crutcher, R. M. 1999, *ApJ*, 520, 706
- Dauphas, N., et al. 2008, *Lunar Planet. Sci. Conf.*, XXXIX, #1170
- Desch, S. J., Connolly, H., & Srinivasan, G. 2004, *ApJ*, 602, 528
- Desch, S. J., & Ouellette, N. 2006, *Geochim. Cosmochim. Acta*, 70, 5426
- Ellinger, C. I., Young, P. A., & Desch, S. J. 2009, *Meteoritical Society Meeting*, Nancy, France, abstract #5385
- Foster, P. N., & Boss, A. P. 1996, *ApJ*, 468, 784
- . 1997, *ApJ*, 489, 346
- Frank, A., & Mellema, G. 1994, *A&A*, 289, 937
- Gaidos, E., Krot, A. N., Williams, J. P., & Raymond, S. N. 2009, *ApJ*, 696, 1854
- Gilmour, J. D., & Middleton, C. A. 2009, *Icarus*, 201, 821
- Goswami, J. N., & Vanhala, H. A. T. 2000, in *Protostars & Planets IV*, ed. V. Mannings, A. P. Boss, & S. S. Russell (Tucson, AZ: Univ. Arizona Press), 963
- Gounelle, M., & Meibom, A. 2007, *ApJ*, 664, L123
- Gounelle, M., Meibom, A., Hennebelle, P., & Inutsuka, S.-I. 2009, *ApJ*, 694, L1
- Gounelle, M., et al. 2001, *ApJ*, 548, 1051
- Halliday, A. 2004, *Nature*, 431, 253
- Healey, K. R., Hester, J. J., & Claussen, M. J. 2004, *ApJ*, 610, 835
- Hester, J. J., & Desch, S. J. 2005, in *ASP Conf. Ser.* 341, *Chondrites and the Protoplanetary Disk*, ed. A. N. Krot, E. R. D. Scott, & B. Reipurth (San Francisco, CA; ASP), 107
- Huss, G. R., et al. 2009, *Geochim. Cosmochim. Acta*, 73, 4922
- Kaufman, M. J., & Neufeld, D. A. 1996, *ApJ*, 456, 611
- Krot, A. N., Yurimoto, H., Hutcheon, I. D., & MacPherson, G. J. 2005, *Nature*, 434, 998
- Krot, A. N., et al. 2008, *ApJ*, 672, 713

- Kudoh, T., & Basu, S. 2008, *ApJ*, 679, L97
- Kunz, M. W., & Mouschovias, T. Ch. 2009, *MNRAS*, 399, L94
- Lee, H.-T., & Chen, W. P. 2009, *ApJ*, 694, 1423
- Lee, T., Papanastassiou, D. A., & Wasserburg, G. J. 1976, *Geophys. Res. Lett.*, 3, 109
- Lee, T., et al. 1998, *ApJ*, 506, 898
- Leppanen, K., Liljestrom, T., & Diamond, P. 1998, *ApJ*, 507, 909
- Looney, L. W., Tobin, J. J., & Fields, B. D. 2006, *ApJ*, 652, 1755
- MacPherson, G. J., Davis, A. M., & Zinner, E. K. 1995, *Meteor.*, 30, 365
- Marchenko, S. V., Moffat, A. F. J., St-Louis, N., & Fullerton, A. W. 2006, *ApJ*, 639, L175
- McKeegan, K. D., Chaussidon, M., & Robert, F. 2000, *Science*, 289, 1334
- McKeegan, K. D., & Davis, A. M. 2003, in *Treatise on Geochemistry*, Vol. 1, ed. A. M. Davis (Amsterdam: Elsevier), 431
- McKeegan, K. D., et al. 2008, *Lunar Planet. Sci. Conf. XXXIX*, #2020
- Melioli, C., de Gouveia Dal Pino, E. M., de la Reza, R., & Raga, A. 2006, *MNRAS*, 373, 811
- Meyer, B. S., & Clayton, D. D. 2000, *Space Sci. Rev.*, 92, 133
- Morris, M. A, Desch, S. J., & Ciesla, F. J. 2009, *ApJ*, 691, 320
- Mouschovias, T. Ch., Tassis, K., & Kunz, M. W. 2006, *ApJ*, 646, 1043
- Nakamura, F., McKee, C. F., Klein, R. I., & Fisher, R. T. 2006, *ApJS*, 164, 477
- Neufeld, D. A., & Kaufman, M. J. 1993, *ApJ*, 418, 263
- Nittler, L. R. 2007, *Workshop on Chronology of Meteorites, Kauai, Hawaii*, #4016
- Oey, M. S., Watson, A. M., Kern, K., & Walth, G. L. 2005, *AJ*, 129, 393
- Ouellette, N., Desch, S. J., & Hester, J. J. 2007, *ApJ*, 662, 1268
- Ouellette, N., et al. 2009, *Geochim. Cosmochim. Acta*, 73, 4946
- Patnaude, D. J., et al. 2002, *AJ*, 124, 2118
- Plait, P., & Soker, N. 1990, *AJ*, 99, 1883
- Poludnenko, A. Y., Frank, A., & Blackman, E. G. 2002, *ApJ*, 576, 832
- Preibisch, T., & Zinnecker, H. 1999, *AJ*, 117, 2381
- Preibisch, T., et al. 2002, *AJ*, 124, 404
- Rauscher, T., Heger, A., Hoffman, R. D., & Woosley, S. E. 2002, *ApJ*, 576, 323

- Regelous, M., Elliott, T., & Coath, C. 2008, *Lunar Planet. Sci. Conf. XXXIX*, #2479
- Rugel, G., et al. 2009, *Phys. Rev. Lett.*, 103, in press
- Russell, S. S., et al. 1996, *Science*, 273, 757
- Sahijpal, S., & Goswami, J. N. 1998, *ApJ*, 509, L137
- Sahijpal, S., & Gupta, G. 2009, *Meteor. Planet. Sci.*, 44, 879
- Sahijpal, S., et al. 1998, *Nature*, 391, 559
- Sandell, G. & Knee, L. B. G. 2001, *ApJ*, 546, L49
- Shirley, Y. L., et al. 2005, *ApJ*, 632, 982
- Shu, F. H., Shang, H., Glassgold, A. E., & Lee, T. 1997, *Science*, 277, 1475
- Snider, K. D., et al. 2009, *ApJ*, 700, 506
- Srinivasan, G., Sahijpal, S., Ulyanov, A. A., & Goswami, J. N. 1996, *Geochim. Cosmochim. Acta*, 60, 1823
- Stone, J. M., & Gardiner, T. 2007, *ApJ*, 671, 1726
- Stone, J. M., & Norman, M. L. 1992, *ApJ*, 390, L17
- Tachibana, S., & Huss, G. R. 2003, *ApJ*, 588, L41
- Tachihara, K., et al. 2002, *A&A*, 385, 909
- Takigawa, A., et al. 2008, *ApJ*, 688, 1382
- Thrane, K., Bizzarro, M., & Baker, J. A. 2006, *ApJ*, 646, L159
- Trigo-Rodríguez, J. M., et al. 2009, *Meteorit. & Planet. Sci.*, 44, 627
- Truelove, J. K., et al. 1997, *ApJ*, 489, L179
- Vanhala, H. A. T., & Boss, A. P. 2000, *ApJ*, 538, 911
- . 2002, *ApJ*, 575, 1144
- Vanhala, H. A. T., & Cameron, A. G. W. 1998, *ApJ*, 508, 291
- Wadhwa, M., et al. 2007, in *Protostars & Planets V*, ed. B. Reipurth, D. Jewitt, & K. Keil (Tucson, AZ: Univ. Arizona Press), 835
- Wasserburg, G. J., Busso, M., Gallino, R., & Raiteri, C. M. 1994, *ApJ*, 424, 412
- Wasserburg, G. J., Gallino, R., & Busso, M. 1998, *ApJ*, 500, L189
- Wasserburg, G. J., et al. 1995, *ApJ*, 440, L101
- Whalen, D. J., & Norman, M. L. 2008, *ApJ*, 672, 287
- Williams, J. P., & Gaidos, E. 2007, *ApJ*, 663, L33

Williams, J. P., Andrews, S. M., & Wilner, D. J. 2005, *ApJ*, 634, 495

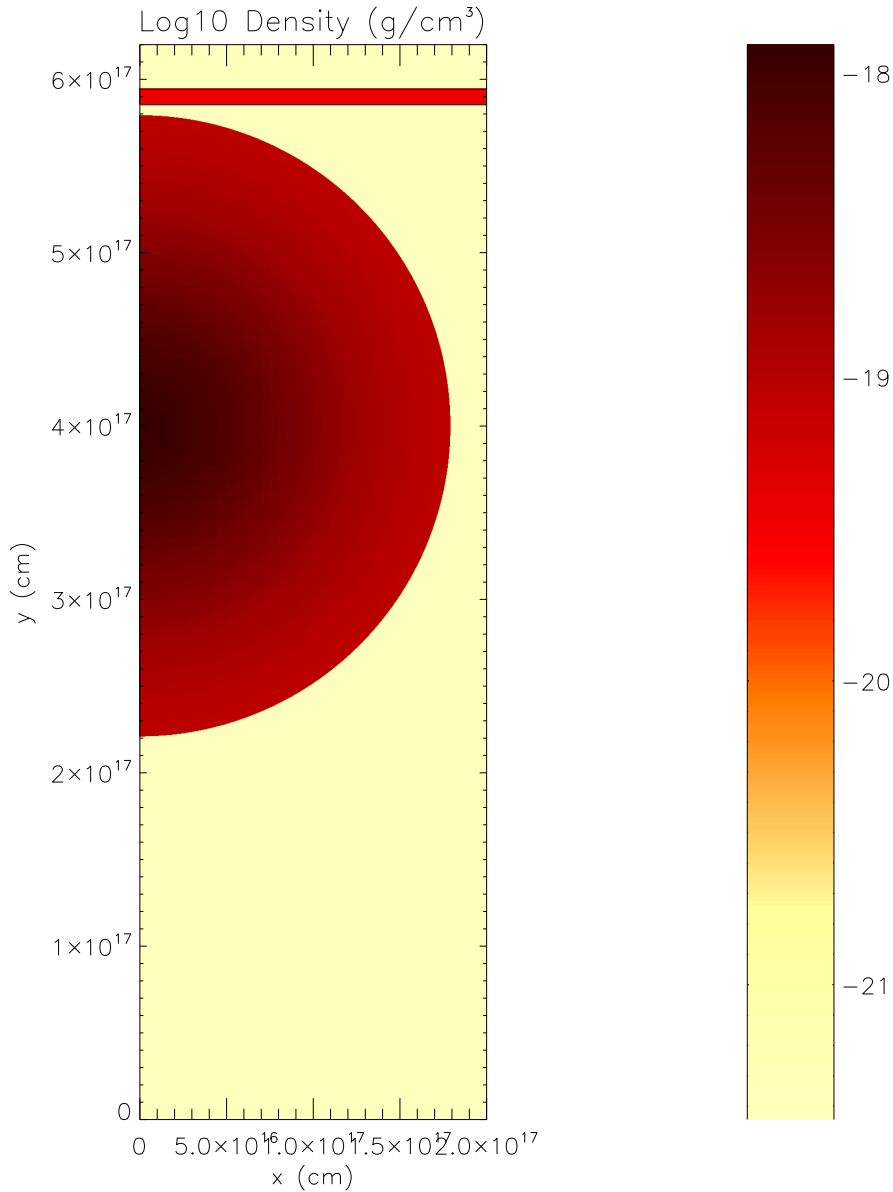
Yokogawa, S., et al. 2003, *ApJ*, 595, 266

Table 1. Comparisons with the standard case of Foster & Boss (1996).

Model	N_{BR}	N_{BZ}	N_L	ρ_{max}	f_i	t_f
FBA	5	5	5	5.3e-13	0.005	5.0e12
FBB	5	10	5	1.7e-12	0.003	4.8e12
FBC	5	10	6	8.0e-12	0.002	4.7e12
FBD	5	15	5	2.0e-12	0.002	4.3e12

Table 2. Nonisothermal models with varied shock speeds.

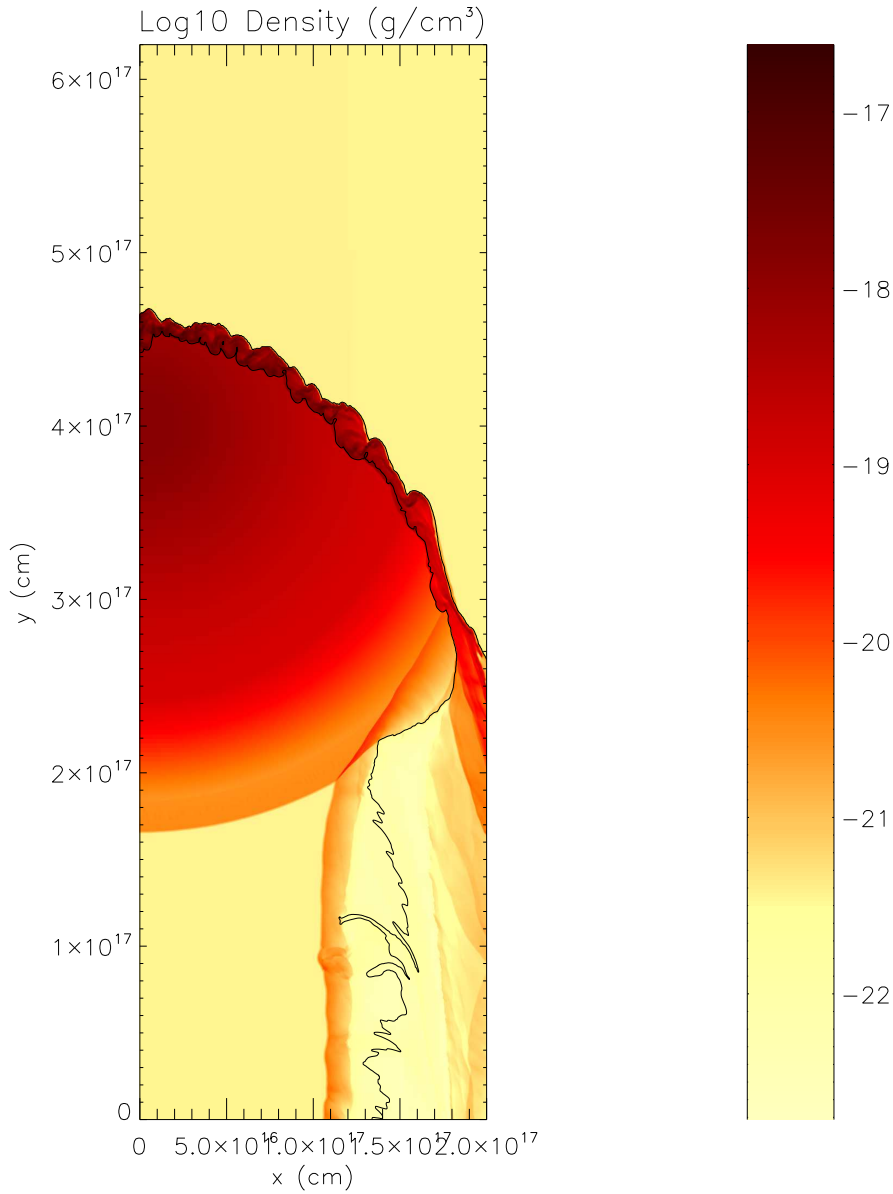
Model	v_s	N_{BR}	N_{BZ}	N_L	ρ_{max}	f_i	t_f
v1	1.0	5	15	5	5.e-12	0.0	3.8e12
v2	2.0	5	15	5	1.e-12	0.0	8.5e12
v2.5	2.5	5	15	5	2.e-12	0.0	4.8e12
v4-4	4.0	5	15	4	1.e-12	0.0	1.2e12
v4	4.0	5	15	5	5.e-12	0.0	3.6e12
v5-4	5.0	5	15	4	2.e-12	2.e-4	7.5e12
v5	5.0	5	15	5	1.e-12	3.e-4	8.5e12
v7	7.0	5	15	5	2.e-12	6.e-4	8.5e12
v9	9.0	5	15	5	1.e-12	2.e-4	1.2e12
v10	10.0	5	15	5	5.e-12	2.e-3	6.5e12
v20	20.0	5	15	5	1.e-12	1.e-3	5.3e12
v20-6	20.0	5	15	6	1.e-12	4.e-4	5.2e12
v30	30.0	5	15	5	4.e-12	3.e-3	4.0e12
v40	40.0	5	15	5	2.e-12	1.e-3	1.2e13
v50	50.0	5	15	5	1.e-12	4.e-4	4.7e12
v60	60.0	5	15	5	1.e-12	4.e-4	6.5e12
v70	70.0	5	15	5	1.e-12	3.e-4	6.5e12
v75	75.0	5	20	5	3.e-13	3.e-4	8.5e12
v75L	75.0	5	20	5	1.e-15	6.e-4	4.5e12
v80L	80.0	5	20	5	1.e-15	5.e-4	3.7e12
v90L	90.0	5	20	5	1.e-15	4.e-4	3.4e12
v100L	100.0	5	20	5	1.e-15	6.e-4	3.0e12



time = 0.000 ps
number of blocks = 3251, AMR levels = 5

/home/flash/FLASH2.5/2d-2m-cool-v20-1000w-15/2d-sc_hdf5_chk_0000

Fig. 1.— Initial log density distribution for all the nonisothermal models (Table 2) with varied shock speeds. Black contours show regions with color fields (representing SLRI) greater than 0.001 (dimensionless units) within the shock wave, which is moving downward from the top of the box and is about to strike the target cloud. The symmetry axis is along the left hand side of the plot. The R axis is horizontal and the Z axis is vertical.

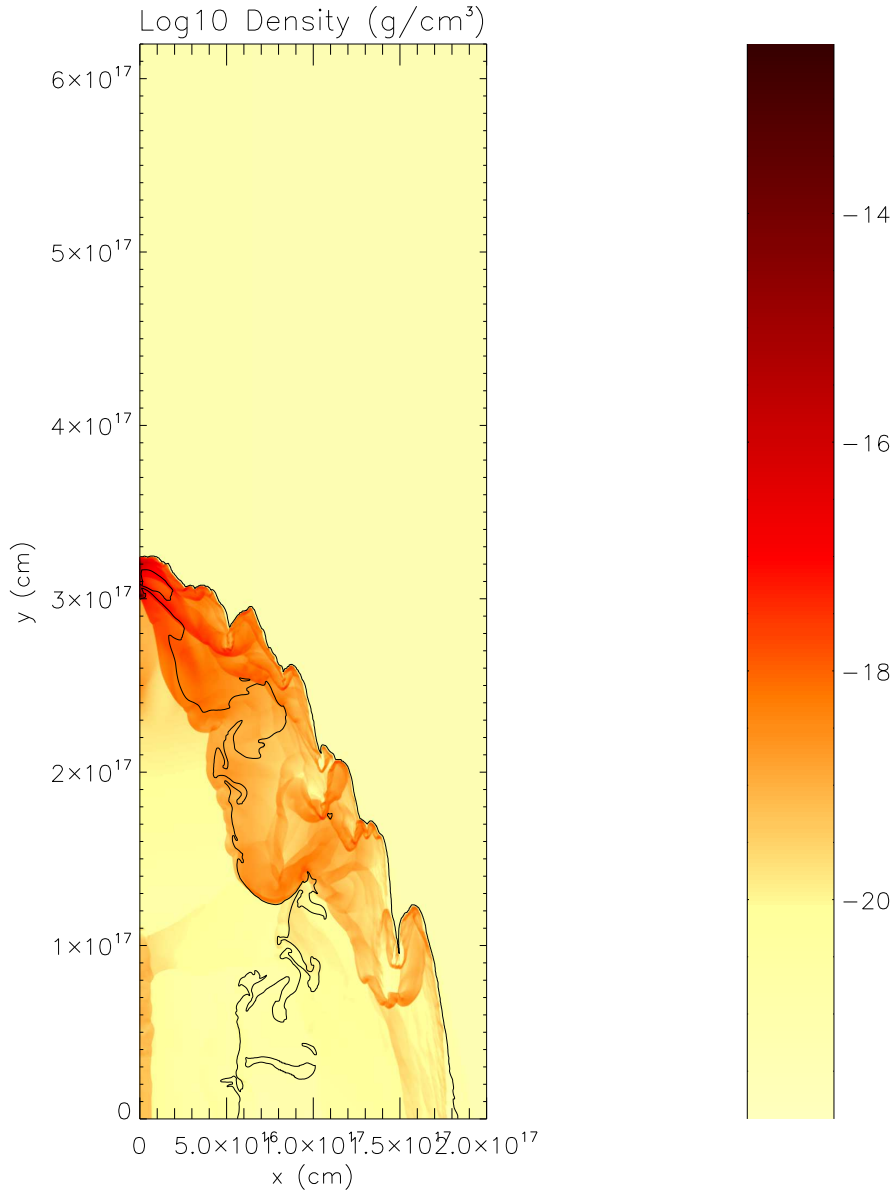


time = 29947.314 years

number of blocks = 8591, AMR levels = 5

/home/flash/FLASH2.5/2d-2m-cool-v20-1000w-15/2d-sc_hdf5_chk_0005

Fig. 2.— Model v20 after 29,947 yr, plotted in the same manner as in Figure 1. R-T fingers and K-H vortices have formed at the shock-cloud interface, simultaneously injecting some shock wave material into the target cloud while ablating other portions of the cloud into the downstream flow.

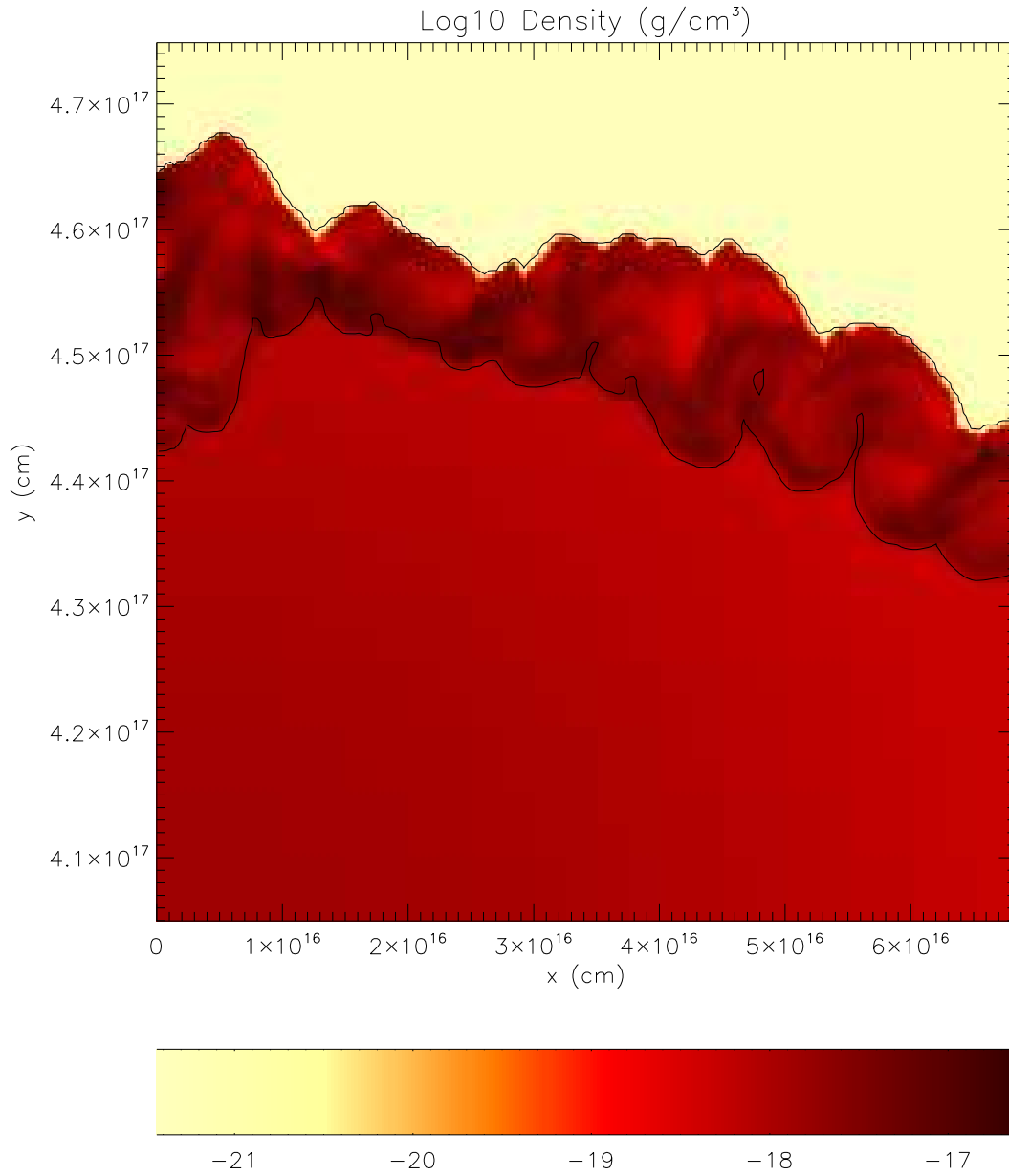


time = 98497.859 years

number of blocks = 8403, AMR levels = 5

/home/flash/FLASH2.5/2d-2m-cool-v20-1000w-15/2d-sc_hdf5_chk_0020

Fig. 3.— Model v20 after 98,498 yr, showing the formation of a dense, dynamically collapsing protostar on the symmetry axis at the middle of the box.

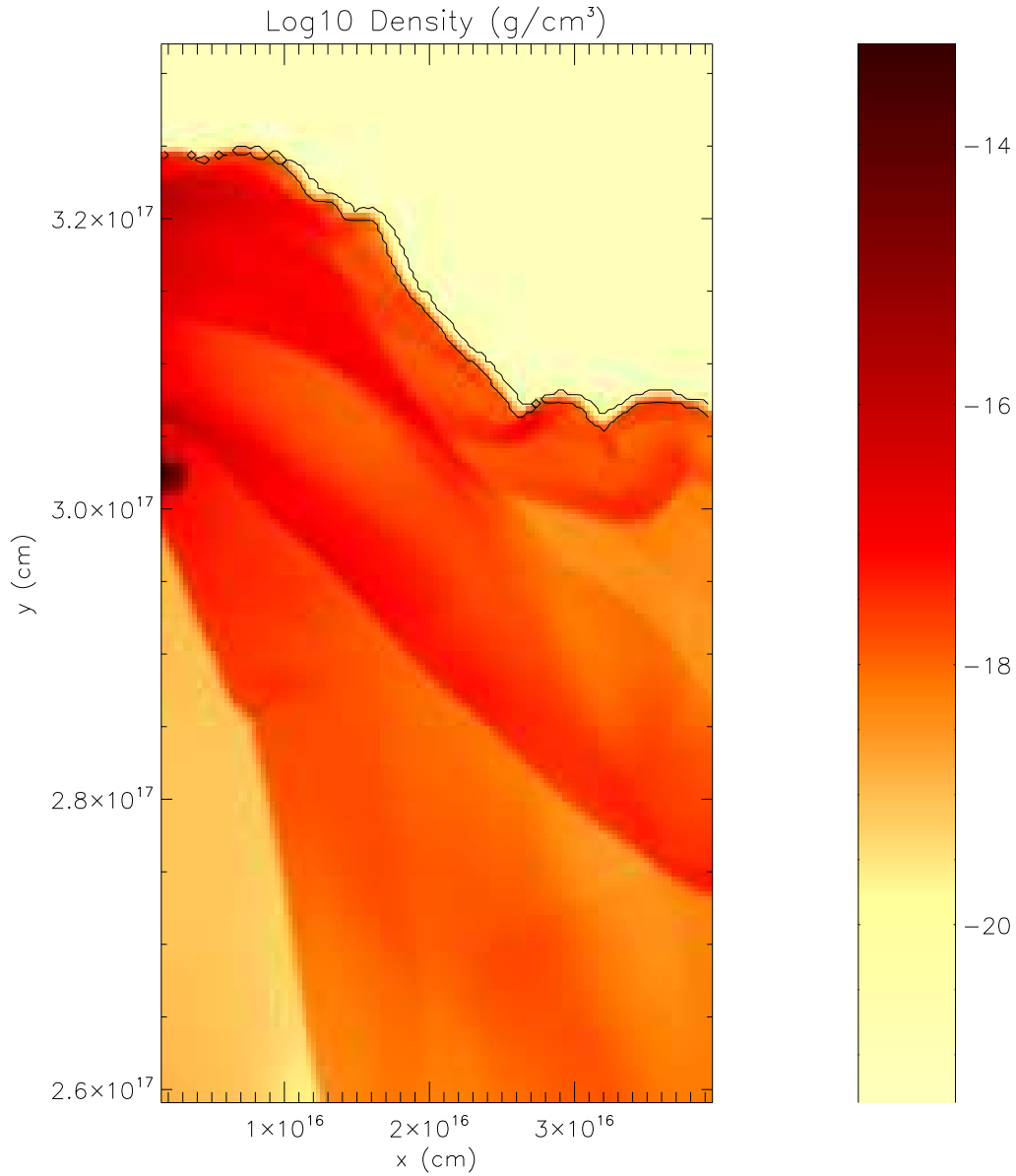


time = 29947.314 years

number of blocks = 8591, AMR levels = 5

/home/flash/FLASH2.5/2d-2m-cool-v20-1000w-15/2d-sc_hdf5_chk_0005

Fig. 4.— Model v20 after 29,947 yr, showing the region around the shock front. The R-T fingers and K-H vortices contain the shock front material, as they lie within the black contour lines for the color field.

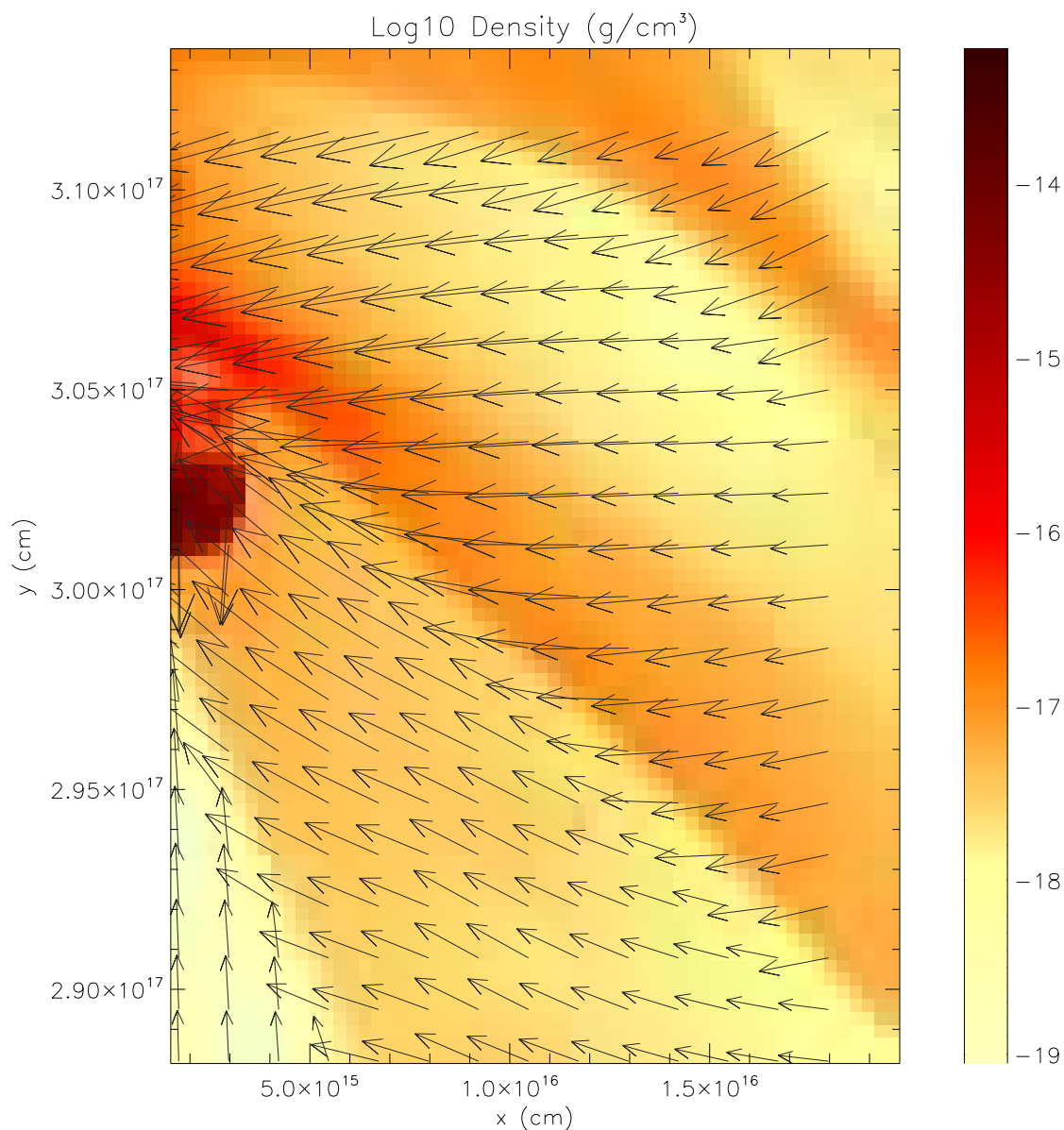


time = 98497.859 years

number of blocks = 8403, AMR levels = 5

/home/flash/FLASH2.5/2d-2m-cool-v20-1000w-15/2d-sc_hdf5_chk_0020

Fig. 5.— Model v20 after 98,498 yr, showing the region around the collapsing protostar. The black contours now show regions with temperatures greater than 100 K, which only occur at the shock-cloud interface as a result of the molecular cooling. A high-density region, the protostar, has formed along the symmetry axis.

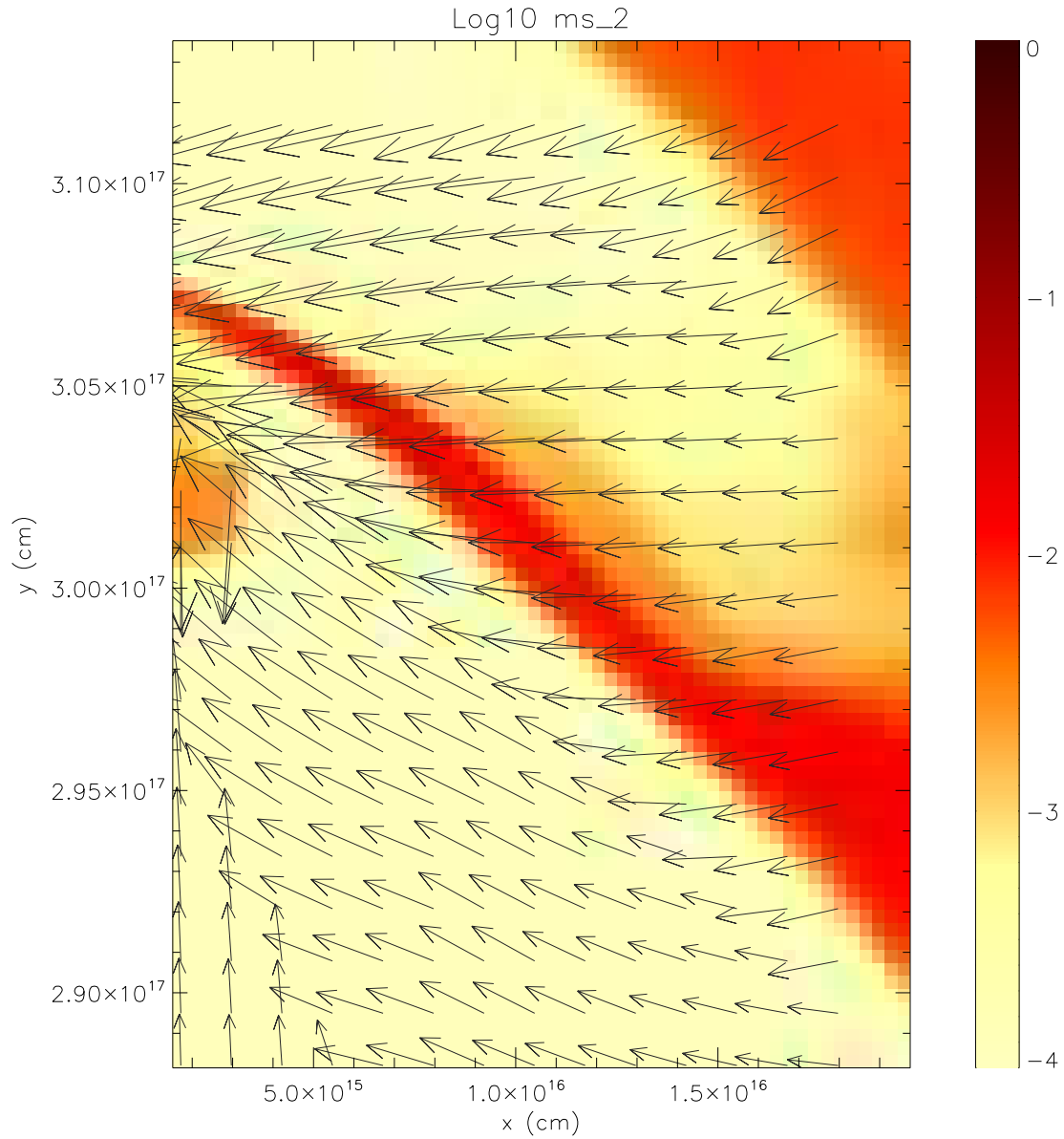


time = 98497.859 years
 number of blocks = 8403, AMR levels = 5

↑
 1.0x10⁵ cm/s
 →

/home/flash/FLASH2.5/2d-2m-cool-v20-1000w-15/2d-sc_hdf5_chk_0020

Fig. 6.— Model v20 after 98,498 yr, as in Figure 5, except limited to a small region around the density maximum of $\sim 10^{-13}$ g cm $^{-3}$. Velocity vectors are shown for every fourth AMR grid cell in R and Z ; their scale bar is 1 km/sec. The collapsing protostar has been accelerated by the shock front into downward motion at a speed of ~ 1 km/sec, while much of the rest of the cloud envelope is infalling toward the growing protostar.

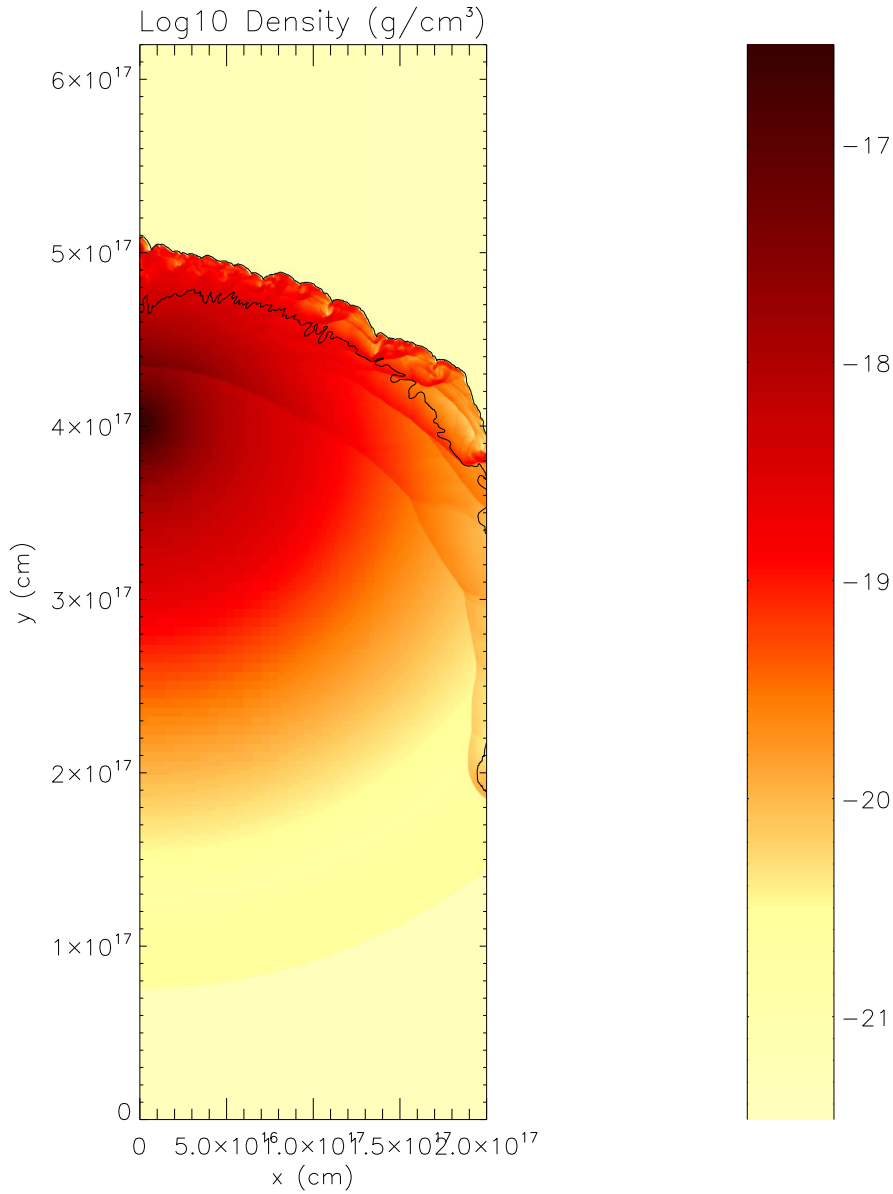


time = 98497.859 years
number of blocks = 8403, AMR levels = 5

↑
1.0x10⁵ cm/s
→

/home/flash/FLASH2.5/2d-2m-cool-v20-1000w-15/2d-sc_hdf5_chk_0020

Fig. 7.— Same as Figure 6 for model v20, except now the log of the color field is plotted, showing that the collapsing protostar has been injected with significant material derived from the shock front, i.e. SLRI. Several waves of color-rich material appear to be headed toward the protostar.

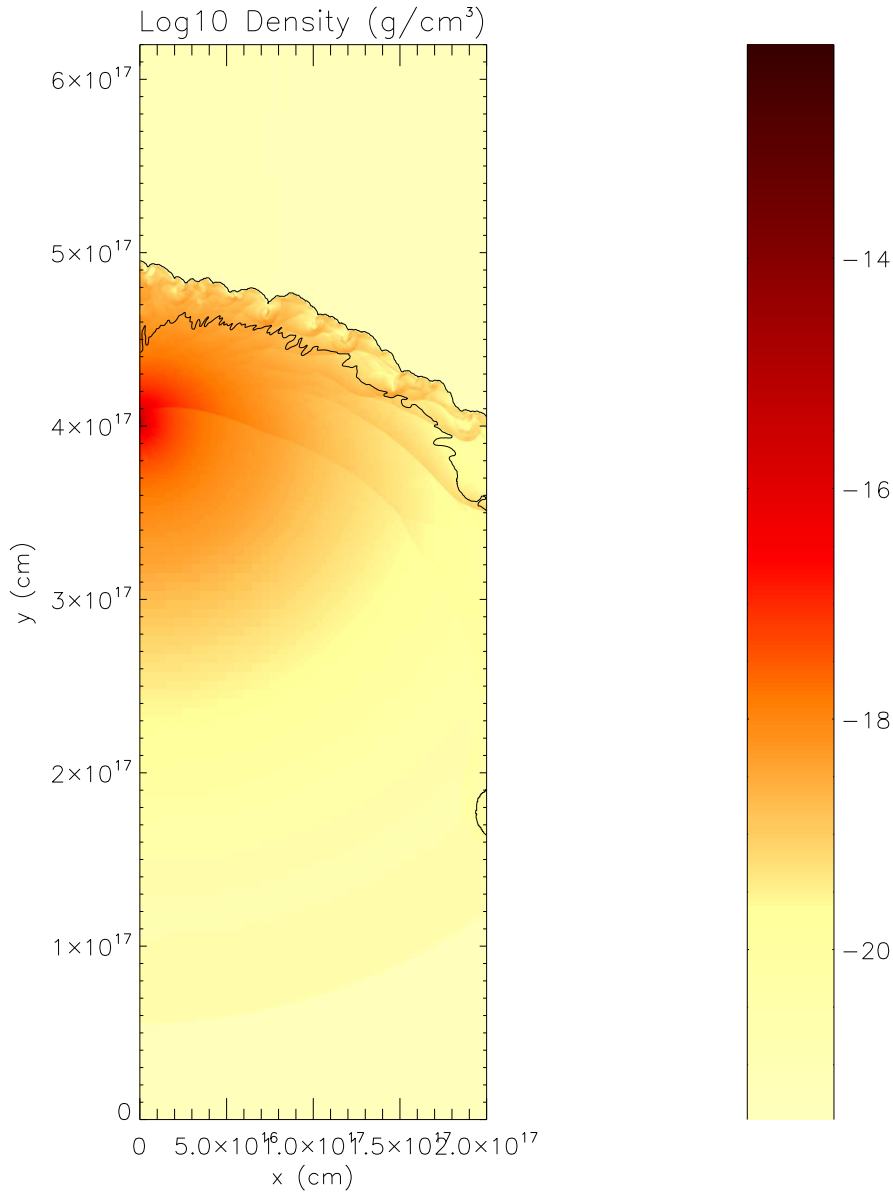


time = 89855.492 years

number of blocks = 6683, AMR levels = 5

/home/flash/FLASH2.5/2d-2m-cool-v4-1000w-15/2d-sc_hdf5_chk_0010

Fig. 8.— Density distribution for model v4 after 89,855 yr of evolution, plotted as in Figure 1, with regions where the color field is greater than 0.001 being denoted by the black contour lines.

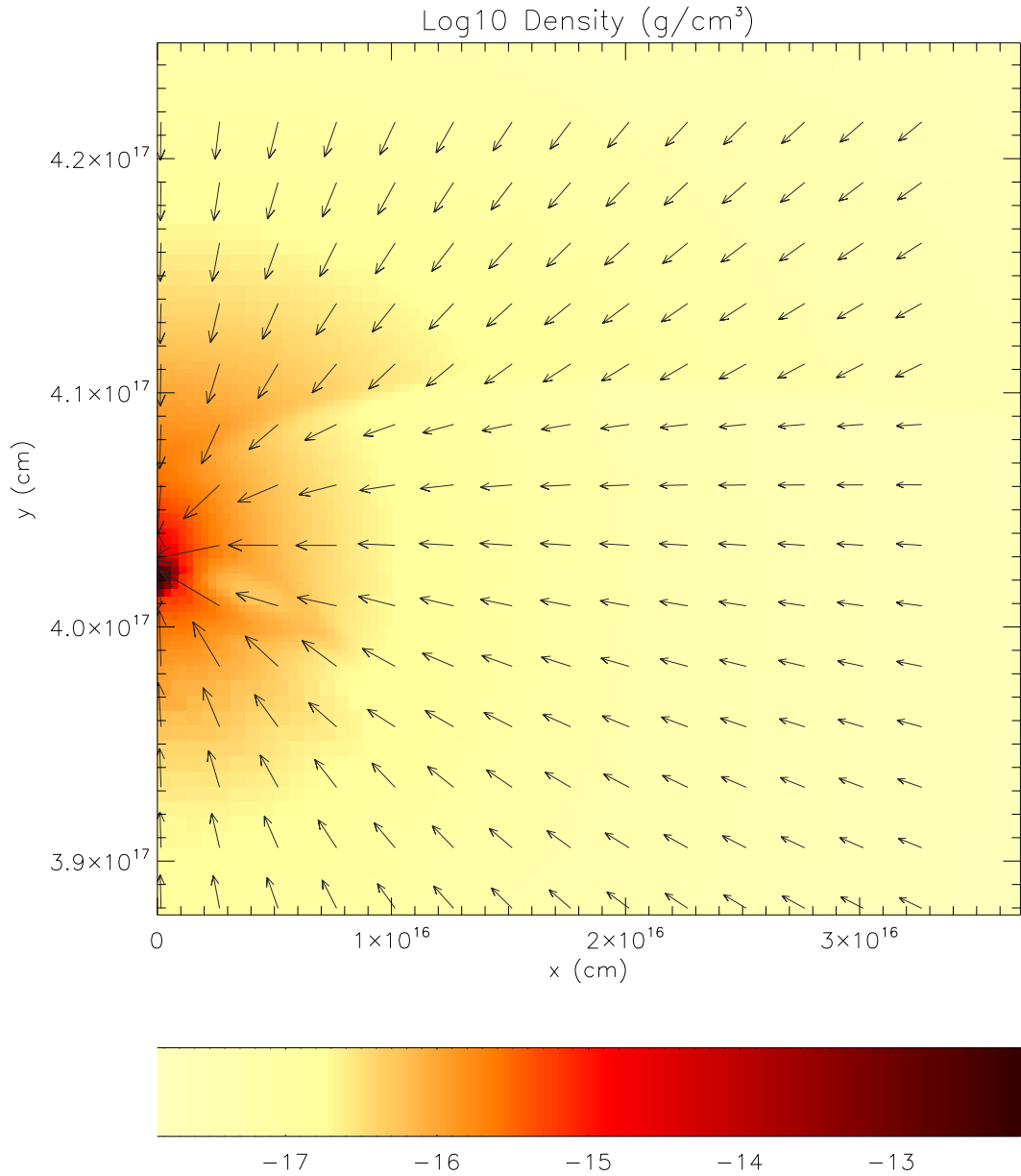


time = 105003.109 years

number of blocks = 6435, AMR levels = 5

/home/flash/FLASH2.5/2d-2m-cool-v4-1000w-15/2d-sc_hdf5_chk_0012

Fig. 9.— Model v4 after 105,003 yr. Compared to Figure 3 for model v20, it is clear that the shock front material has not been able to penetrate into the densest regions of the collapsing target cloud, though some of the color field might be injected at later times.



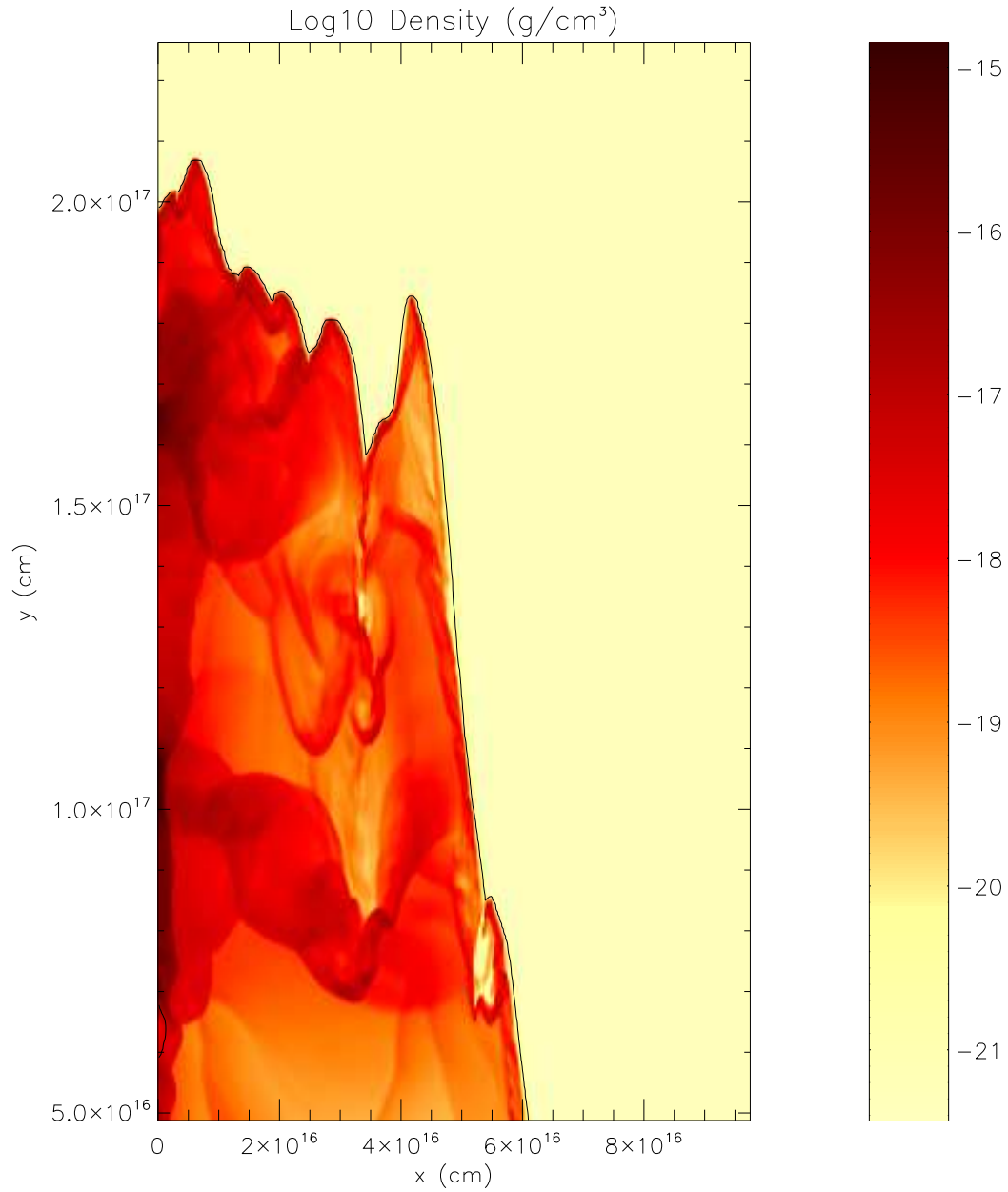
time = 105003.109 years

number of blocks = 6435, AMR levels = 5

1.0×10^5 cm/s

/home/flash/FLASH2.5/2d-2m-cool-v4-1000w-15/2d-sc_hdf5_chk_0012

Fig. 10.— Model v4 after 105,003 yr, showing the region around the collapsing protostar, with a density maximum of $\sim 10^{-12}$ g cm^{-3} . The color field is effectively zero throughout this region. Velocity vectors are plotted for every eighth AMR grid cell in R and Z . The protostar is collapsing but has not been accelerated downward to a speed of ~ 1 km/sec, as happened with model v20 (Figure 6).

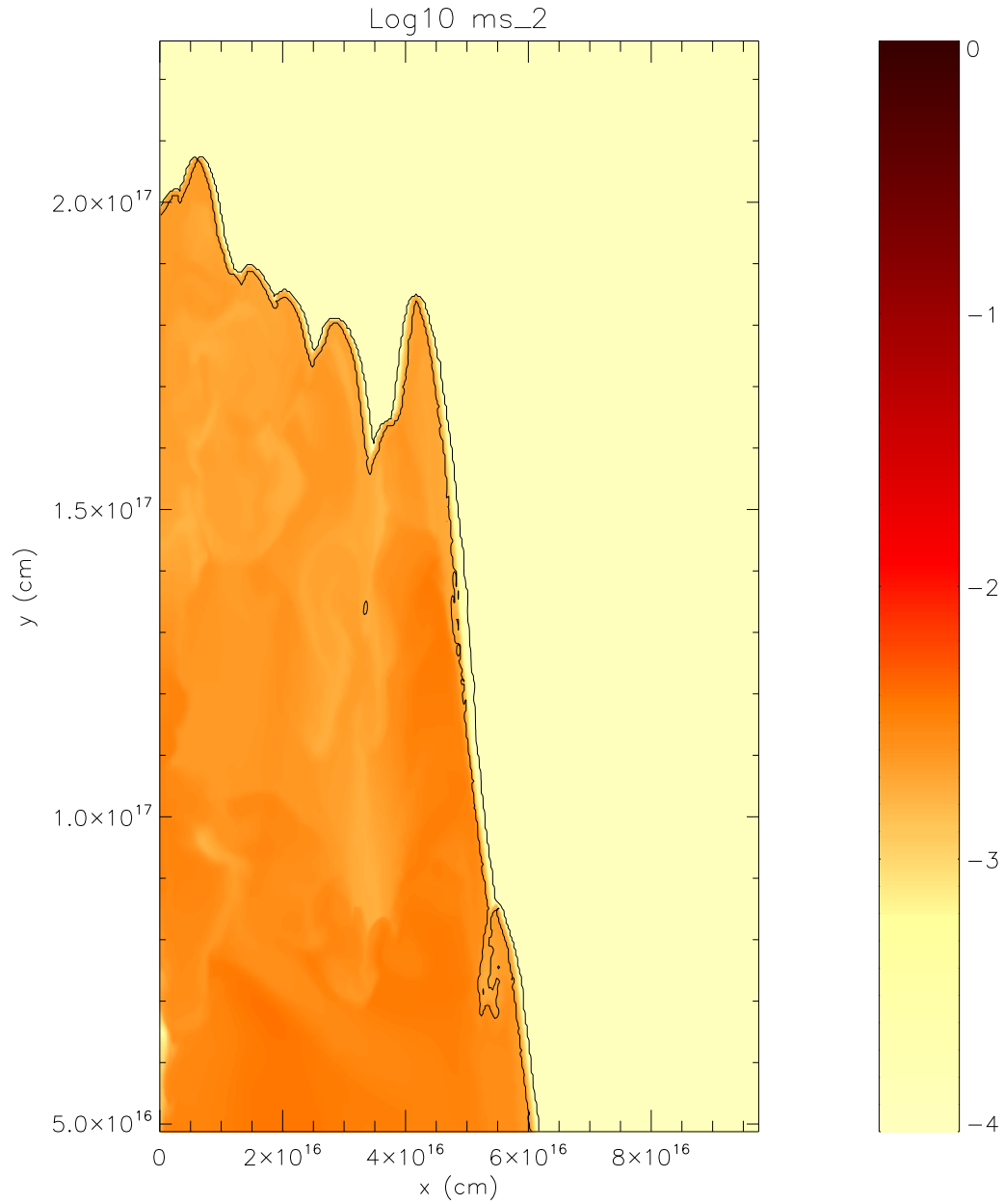


time = 55864.352 years

number of blocks = 10096, AMR levels = 5

/second/dc101/p1/flash/FLASH2.5/2d-2m-cool-v80-1000w-20-5/2d-sc_hdf5_chk_0020

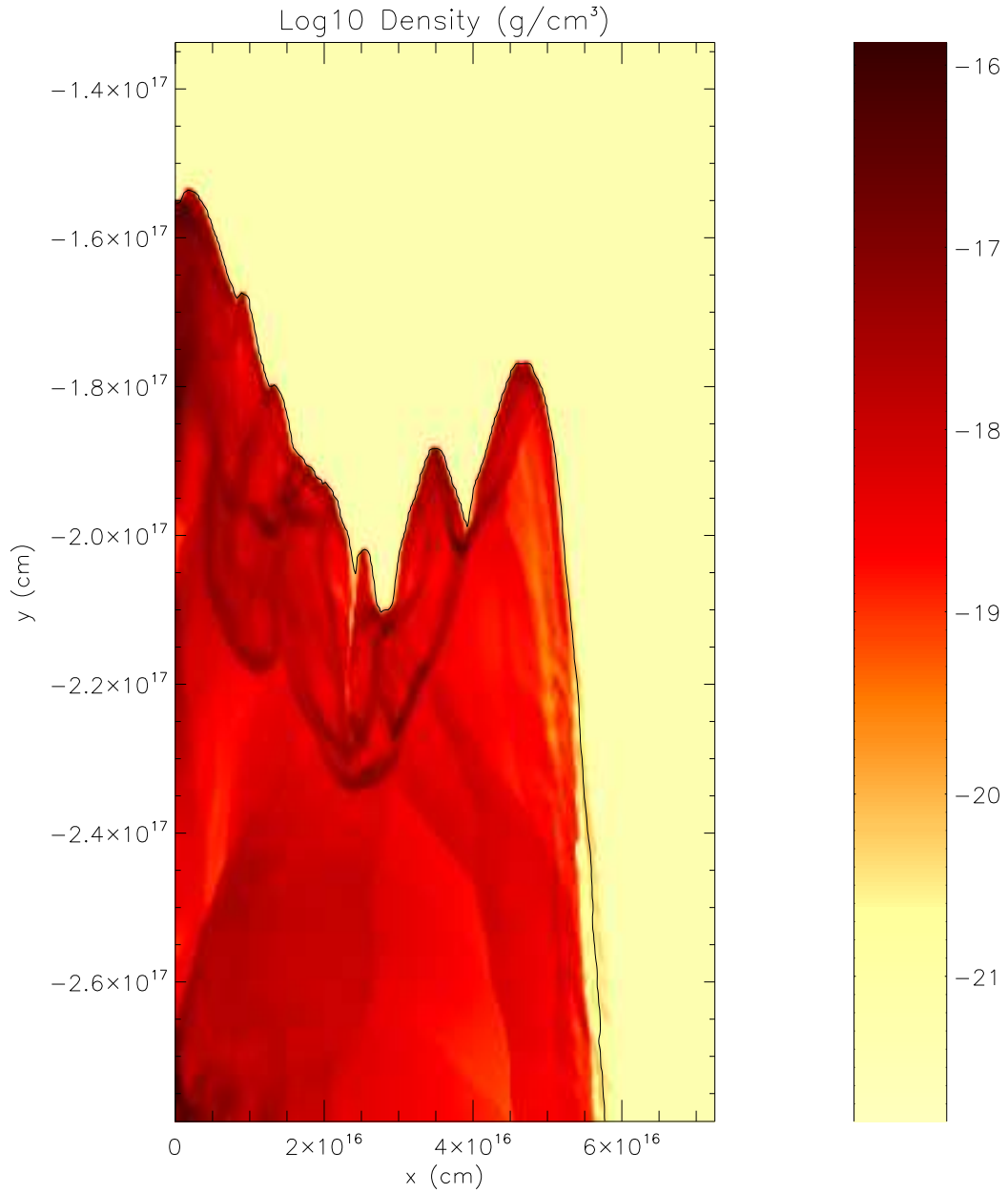
Fig. 11.— Density distribution for model v80 after 55,864 yr of evolution, plotted as in Figure 1, but only for the highest density regions. The target cloud has a much more turbulent structure after being struck with this higher speed shock, compared to the previous models v20 and v4. The density maximum is only $\sim 10^{-15} \text{ g cm}^{-3}$.



time = 55864.352 years
number of blocks = 10096, AMR levels = 5

/second/dc101/p1/flash/FLASH2.5/2d-2m-cool-v80-1000w-20-5/2d-sc_hdf5_chk_0020

Fig. 12.— Model v80 after 55,864 yr, showing the same region as in Figure 11, but plotting the log of the color field and temperature contours (black) for regions with $T > 100\text{K}$. The entire region is polluted with shock wave material. Nonisothermal temperatures are again limited to the edges of the shock-cloud interface.



time = 99886.367 years

number of blocks = 2772, AMR levels = 5

/second/dc101/p1/flash/FLASH2.5/2d-2m-cool-v80-1000w-20-5/2d-sc_hdf5_chk_0029

Fig. 13.— Same as Figure 11 after 99,886 yr for model v80. The density maximum has dropped to $\sim 10^{-16} \text{ g cm}^{-3}$; dynamic collapse leading to protostellar formation has not occurred.

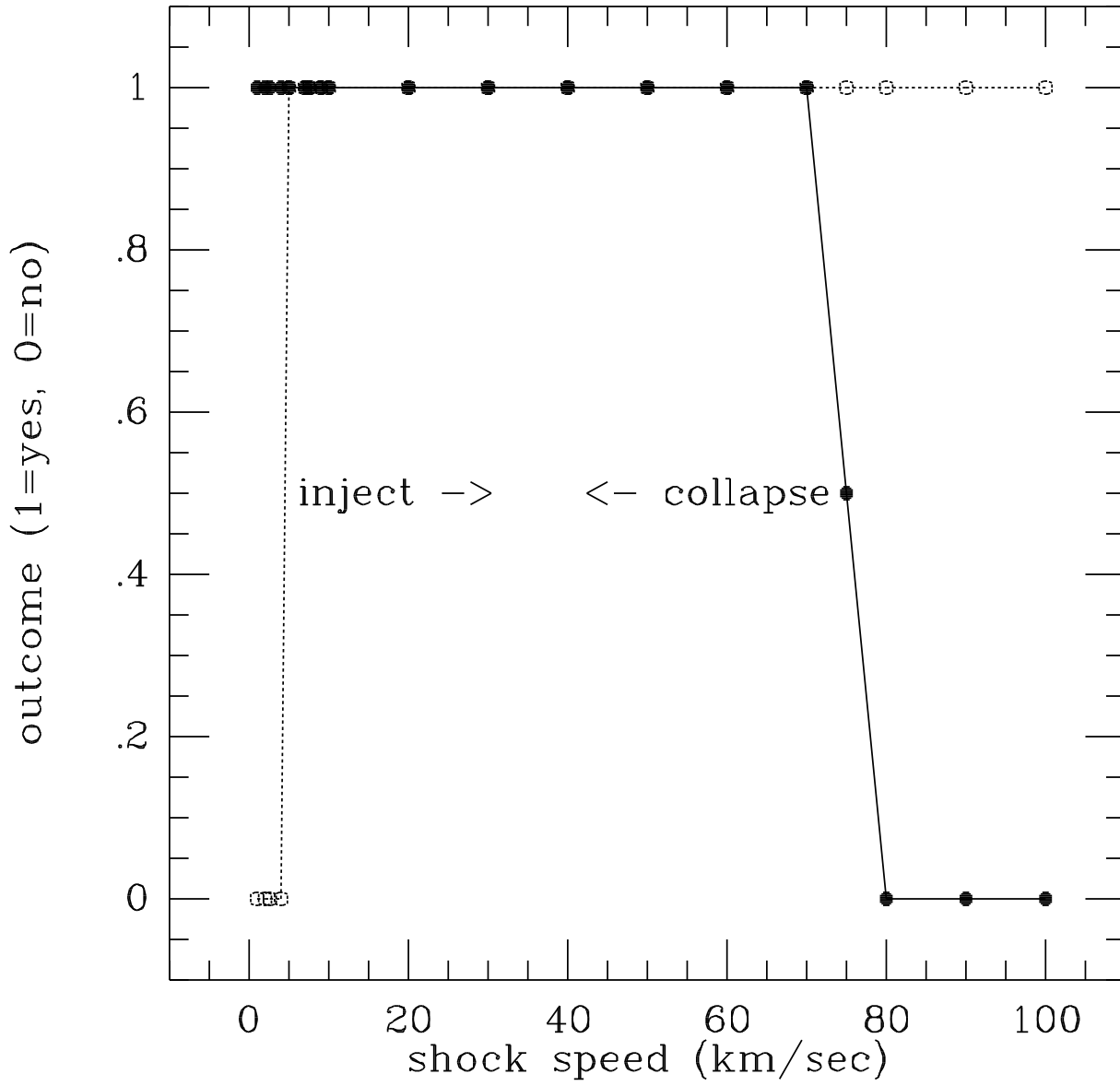


Fig. 14.— Results for the models with varied shock speeds, indicating whether dynamic collapse resulted (filled circles) or whether shock wave material was injected significantly into the dense cloud core (open circles). The overlap of these two criteria represent successful models for shock-triggered collapse and injection.